Cortical depth-dependent human fMRI of resting-state networks using EPIK

1   **Patricia Pais-Roldán[1], Seong Dae Yun[1], Nicola Palomero-Gallagher[2-4], N. Jon Shah[1,5-7] ***

2   [1]Institute of Neuroscience and Medicine 4, Medical Imaging Physics, Forschungszentrum Jülich,
3   Germany
4   [2]Institute of Neuroscience and Medicine 1, Structural and Functional Organisation of the Brain,
5   Forschungszentrum Jülich, Germany
6   [3]C. & O. Vogt Institute for Brain Research, Heinrich-Heine-University, 40225 Düsseldorf, Germany
7   [4]Department of Psychiatry, Psychotherapy and Psychosomatics, Medical Faculty, RWTH Aachen,
8   Aachen, Germany
9   [5]Institute of Neuroscience and Medicine 11, Molecular Neuroscience and Neuroimaging, JARA,
10 Forschungszentrum Jülich, Germany
11 [6]JARA - BRAIN - Translational Medicine, Aachen, Germany
12 [7]Department of Neurology, RWTH Aachen University, Aachen, Germany

13 *** Correspondence:**
14 Prof. N. Jon Shah
15 n.j.shah@fz-juelich.de

16 **Keywords: Cerebral cortex, Cortical Layer, Resting-state fMRI, High-resolution, EPIK**

17 **Manuscript length**: 9620 words

18 **Number of main figures**: 4 (Number of supplementary figures: 14)

19 **Number of tables**: 1

20 **Conflict of Interest**

21 *The authors declare that the research was conducted in the absence of any commercial or financial*
22 *relationships that could be construed as a potential conflict of interest.*

23 **Author Contributions**
24 *N.J.S. designed the research; S.Y. developed the MR imaging sequence and the corresponding image*
25 *reconstruction software; S.Y. and P.P. performed in vivo experiments. P.P. designed and performed*
26 *data analysis; P.P. wrote the manuscript and prepared figures; N.J.S. invented the original EPIK*
27 *sequence; N.P.-G. verified the anatomical labels and wrote the cytoarchitecture-related discussions;*
28 *S.Y., N.P.-G. and N.J.S. reviewed the manuscript.*

33 **Data Availability Statement**

34 *The original* in vivo *data from 13 subjects can be shared by submitting a formal request to the*
35 *corresponding author (N. Jon Shah: n.j.shah@fz-juelich.de). The general protection of personal data*
36 *and privacy policy, declared by the Council of Europe (https://www.coe.int/en/web/portal/personal-*

37   *data-protection-and-privacy), applies to health-related data (CM/Rec(2019)2). The protection of* in

38   vivo *data or metadata derived from the original data is further described by the corresponding*

39   *ethics/internal administrating documents. The sharing is based on the consent of the subject whose*

40   *data are to be shared; these subjects will be informed beforehand.*

Abstract

Recent laminar-fMRI studies have substantially improved understanding of the *evoked* cortical responses in multiple sub-systems; in contrast, the laminar component of *resting-state networks* spread over the whole brain has been less studied due to technical limitations. Animal research strongly suggests that the supragranular layers of the cortex play a critical role in maintaining communication within the default mode network (DMN); however, whether this is true in this and other human cortical networks remains unclear. Here, we used EPIK, which offers unprecedented coverage at sub-millimeter resolution, to investigate cortical broad resting-state dynamics with depth specificity in healthy volunteers. Our results suggest that human DMN connectivity is primarily supported by intermediate and superficial layers of the cortex, and furthermore, the preferred cortical depth used for communication can vary from one network to another. This has major implications for the characterization of network-related diseases and should occupy future high-resolution studies. In addition, the laminar connectivity profile of some networks showed a tendency to change upon engagement in a motor task. In line with these connectivity changes, we observed that the amplitude of the low-frequency-fluctuations (ALFF), as well as the regional homogeneity (ReHo), exhibited a different laminar slope when subjects were either performing a task or were in a resting state (less variation among laminae, i.e., lower slope, during task performance compared to rest). The varied laminar profiles concerning network connectivity, ALFF, and ReHo, observed across two brain states (task vs. rest) suggest the potential diagnostic value of laminar fMRI in psychiatric diseases, e.g., to differentiate the cortical dynamics associated with disease stages linked, or not linked, to behavioral changes. The evaluation of laminar-fMRI across the brain encompasses computational challenges; nonetheless, it enables the investigation of a new dimension of the human neocortex, which may be key to understanding neurological disorders from a novel perspective.

65   ## 1. INTRODUCTION

66

67   In the mammalian brain, the cerebral cortex is organized into specialized functional areas across its surface. In
68   humans, the largest part of the cerebral cortex is occupied by the neocortex, where the perikarya of multiple
69   neuronal cell types are organized into six horizontal layers. The layered structure of the neocortex, which can
70   be characterized by its cytoarchitecture, is involved in specialized signal processing (Palomero-Gallagher and
71   Zilles, 2019, Thomson and Bannister, 2003, Larkum et al., 2018). The functional specificity of the cortex at its
72   different depths has been demonstrated in animals using multi-site electrodes and, more recently, with cell-
73   specific calcium imaging, e.g., via two-photon microscopy or optical fibers (Michelson and Kozai, 2018, Krupa
74   et al., 2004, Adesnik and Naka, 2018, Ayaz et al., 2019, Scott et al., 2018). Although electrophysiology can
75   theoretically be performed in the human brain to investigate layer-specific activations, it is an extremely invasive
76   technique, and, consequently, data are only available from select patient groups, e.g., in epileptic patients, who
77   benefit from such an undertaking (Csercsa et al., 2010). Moreover, although electrode recordings can provide
78   direct information concerning layer activity, the coverage of electrophysiological recordings is limited by the
79   number of multi-site electrodes, which is usually a single point at different depths. In contrast to the limitations
80   of electrophysiology, functional magnetic resonance imaging (fMRI) can afford broad brain coverage non-
81   invasively, although it is usually limited by relatively low temporal and spatial resolution. In rodents,
82   experiments merging fMRI and axonal tracing maps demonstrated that layers 2/3, but not other cortical depths,
83   project exclusively to areas within the default mode network (DMN) (Whitesell et al., 2021), and it has been
84   shown that stimulation of upper, but not lower, sections of the motor cortex results in network-wide effects
85   (Weiler et al., 2008), suggesting a primary role of the superficial cortical laminae in resting-state networking.
86   Due to a lack of non-invasive methods to sufficiently sample the cerebral cortex, the specific way in which the
87   cortical neurons communicate with each other in the human brain -across different depths and through different
88   areas- largely remains an open challenge, which could be addressed with novel high-resolution fMRI methods.

89

90   fMRI most commonly relies on the identification of blood changes, which, assuming perfect neuro-vascular
91   coupling, represent neuronal function in the brain (Logothetis et al., 2001, Logothetis, 2002, Ogawa et al., 1990).
92   Despite its dependence on the vascular architecture of the cortex, laminar fMRI, i.e. sub-millimeter resolution
93   fMRI acquired with the purpose of studying depth-specific neuronal responses, has proven to be a valuable tool
94   for studying cortical dynamics in animals and humans (for a review of methods and applications, see references
95   (Lawrence et al., 2019, Petridou and Siero, 2019, Scheeringa and Fries, 2019, Huber et al., 2021a)). Two main
96   fMRI contrasts are usually employed in human laminar fMRI: cerebral blood volume (CBV), typically applied
97   as part of vascular occupancy schemes (VASO), and blood oxygenation level dependent (BOLD). Although
98   VASO offers high spatial specificity by detecting dilation of the microvasculature based on T1 contrast, it
99   exhibits low sensitivity due to unwanted tissue suppression by an inversion recovery pulse (Lu et al., 2003,
100   Huber et al., 2018, Poplawsky et al., 2015). In contrast, sequences based on BOLD present the advantage of a

101 higher signal-to-noise ratio (SNR), with spin-echo-based (SE) echo planar imaging sequences (EPI) offering
102 greater parenchymal specificity and gradient-echo (GE) schemes offering the best sensitivity [27]. The higher
103 SNR and the flexibility of being able to accommodate higher sampling rates make GE sequences some of the
104 most commonly used in the fMRI field, typically in the form of GE-EPI. Due to GE schemes having enhanced
105 sensitivity to large vessels (Kay et al., 2019), with long T2* constants, e.g., pial veins, several methods have
106 been presented for use in the pre-processing pipeline to ameliorate contamination from extra-parenchymal
107 signals or to correct the evoked activation profile across cortical depths (Menon, 2002, Curtis et al., 2014,
108 Fracasso et al., 2018, Kashyap et al., 2018a, Heinzle et al., 2016, Markuerkiaga et al., 2016, Kay et al., 2020).

110 fMRI acquired with different contrasts and sub-millimeter resolution has enabled the function of the cerebral
111 cortex to be sampled with column- and layer-specificity in the context of sensory, motor, visual, and auditory
112 tasks (Guidi et al., 2016, Huber et al., 2017, Chai et al., 2020, Huber et al., 2015, Siero et al., 2011, Yu et al.,
113 2014, Ress et al., 2007, Polimeni et al., 2010, Kashyap et al., 2018b, van Mourik et al., 2019, De Martino et al.,
114 2015, Muckli et al., 2015, Yacoub et al., 2008) and has shown the superficial layers of the neocortex to be
115 predominantly involved in the processing of neuronal signals. This predominance is possibly due to the fact that
116 layer III is the main source and target of cortico-cortical connectivity (Zilles and Catani, 2020) and that the
117 higher synaptic density found there compared to the remaining cortical layers is associated with higher receptor
118 densities (Palomero-Gallagher and Zilles, 2019). Importantly, a study focusing on the visual cortex reported
119 correlations between the function of specific layers imaged with fMRI and particular EEG rhythms (Scheeringa
120 et al., 2016), reinforcing the potential for using fMRI to detect layer variability.

122 In contrast to task-related circuits, which are usually limited to specialized responses in a small portion of the
123 cerebral cortex, during rest, cross-talk between distant cortical areas maintains a baseline neurological state
124 (Raichle et al., 2001). Although the potential for using fMRI to sample cortical layers is clear, the limited brain
125 coverage enforced by most existing high-resolution-fMRI schemes precludes the investigation of large-scale
126 inter-regional depth-dependent connections; i.e. some resting-state evaluations have been presented previously,
127 but these mostly focused on particular systems, e.g., (Polimeni, 2010, Huber et al., 2017). To date, only a few
128 groups have reported fMRI acquisitions from the whole brain at ≤ 1 mm resolution (De Martino et al., 2011,
129 Sharoh et al., 2019, Huber et al., 2020), and, to our knowledge, only one study has intended to use laminar fMRI
130 to uncover the cross-layer functional interactions that exist in the human brain during rest with a nominal spatial
131 resolution of $0.8 \times 0.8 \times 0.8$ mm^3 (Huber et al., 2020).

133 Here, we applied TR-external EPI with keyhole (EPIK) (Yun et al., 2022) to identify the laminar signals from
134 most of the cerebral cortex with a 0.63 mm iso-voxel size in healthy volunteers. It has been previously shown
135 that EPIK (Shah, 2003, Shah NJ, 2004, Zaitsev et al., 2001, Zaitsev et al., 2005, Yun, 2020, Yun and Shah,
136 2020, Yun et al., 2022) can offer higher spatial resolution in dynamic MR studies with comparable

137 hemodynamic-response detection compared to routine EPI (Yun et al., 2013, Yun and Shah, 2017, Caldeira et

138 al., 2019, Shah et al., 2019, Yun et al., 2019). Moreover, the combination of TR-external phase correction with

139 EPIK has been shown to further enhance spatial resolution (Yun, 2022). In this work, TR-external EPIK covered

140 the human cerebrum almost entirely, with 123 slices sampling voxel volumes of ~ 0.25 mm^3. The combination

141 of a smaller voxel size and near whole-brain coverage is a key feature of this work when compared to previous

142 laminar fMRI studies. By adding pre-processing steps to ameliorate the potential bias of the GE sequence, the

143 acquired images allowed us to perform cortical depth-dependent analysis of broad resting-state networking in

144 the human brain.

145   ## 2. MATERIALS AND METHODS

146

147   ### 2.1. Subjects:

148   The functional data from thirteen healthy volunteers (eleven males and two females; age, 23-47 years; 12/13
149   right-handed, 1/13 left-handed (Schweisfurth et al., 2018)) were included in this study. Although eighteen
150   subjects were originally measured, four of them were removed from the study due to the lack of/non-proper
151   physiological recordings, and an additional set of data was removed after detecting high levels of motion. Hence,
152   the structural scans of eighteen subjects were used for the anatomical study of the cortex, but only data from
153   thirteen subjects were included in the functional analysis relevant to the majority of the results shown in this
154   manuscript. Subjects were scanned in one single session for a period of ~55 min, which included two resting-
155   state fMRI scans ('rs-fMRI-1' and 'rs-fMRI-2'), one finger motor task fMRI scan ('task-fMRI'), and an
156   MP2RAGE scan. Due to poor anatomical-functional co-registration, the rs-fMRI-2 data from one subject were
157   omitted, and another subject was excluded from both the rs-fMRI-2 analysis and the whole-brain laminar
158   evaluations of the task-fMRI for the same reason (i.e. the number of subjects used in the whole-brain analysis
159   were 13, 11 and 12 for rs-fMRI-1, rs-fMRI-2, and task-fMRI, respectively). However, the task-fMRI data from
160   all 13 subjects were used for the analysis of evoked responses in the primary motor cortex (M1) as the motor
161   cortex could be well co-registered in all subjects. A pneumatic belt was positioned around the subject's chest,
162   and a pulse oximeter was placed on the 2nd, 3rd, or 4th finger of the left hand to control for potential interference
163   of the physiological signals on the fMRI responses (Glover et al., 2000). The experimental methods were
164   approved by the local institutional review board (EK 346/17, RWTH Aachen University, Germany), MR-safety
165   screening was performed prior to the MRI acquisition, and informed written consent was obtained from all
166   subjects.

167

168   ### 2.2. Experimental design:

169   In the rs-fMRI, subjects were asked to remain still, awake, with eyes closed, and without thinking about anything
170   in particular. In total, 172 volumes were reconstructed from the rs-fMRI (~10 min). For task-fMRI, subjects
171   were asked to follow instructions on a projected screen and to perform flexion of the right index finger without
172   necessarily touching the thumb. The task was performed continuously at a comfortable pace (1-2 Hz, for most
173   subjects) for 21 s and was repeated 12 times, alternated with 21 s of rest. In total, 148 volumes were obtained (4
174   s rest, [21 s task, 21 s rest] × 12) (~ 8.6 min). One subject was invited to participate in an additional scan session
175   and first performed a finger motor task (4 s rest, [21 s task, 21 s rest] × 8), followed by a finger motor and
176   sensory task, i.e. instructions were given to approach the right index finger towards the thumb involving touching
177   (4 s rest, [21 s task, 21 s rest] × 8).

178

179   ### 2.3. MRI data acquisition:

180   MRI data were collected on a Siemens Magnetom Terra 7T scanner with a 1-channel Tx / 32-channel Rx Nova

181   Medical head coil. An anatomical MRI volume was acquired using an MP2RAGE sequence, TR/TE = 4300/2

182   ms, matrix = $256 \times 376 \times 400$ ($0.60 \times 0.60 \times 0.60$ mm^3). Functional MRI data were obtained using GE-EPIK

183   combined with a TR-external EPI phase correction scheme. The sequence performance has been previously

184   described elsewhere and briefly consists of a full sampling of central k-space (48 central lines) and a sparse

185   sampling of the peripheral k-space (288 lines), which is completely acquired after three TRs, i.e. every TR

186   encompasses the acquisition of the k-space center and 1/3 of the periphery (details of the sequence can be found

187   in previous publications (Yun and Shah, 2017, Yun et al., 2013, Yun et al., 2019, Yun and Shah, 2020, Yun,

188   2022, Yun et al., 2022)). Sampling the central k-space at every TR ensures a near-optimum SNR for each

189   individual scan. An analysis of raw data from a healthy subject in our preliminary study showed that the central

190   k-space in the current configuration has 86.5% of the entire k-space energy, whereas including the peripheral k-

191   space lines that are continuously updated at every scan (i.e. 1/3 of the periphery) results in 91.0% of the entire

192   energy. Two acquisition protocols were used to collect data in this study. In both protocols, TR/TE = 3500/22

193   ms, FA = 85°, partial Fourier = 5/8, 3-fold in-plane/3-fold inter-plane (multi-band) acceleration, bandwidth =

194   875 Hz/Px, and αPC/αMain = 9°/90°. B0 shimming was performed with a standard routine provided by the

195   manufacturer. For protocol-1 (used to generate all the data in the main figures), matrix = $336 \times 336 \times 123$ slices

196   ($0.63 \times 0.63 \times 0.63$ mm^3). For protocol-2, matrix = $408 \times 408 \times 105$ slices ($0.51 \times 0.51 \times 1.00$ mm^3). The main

197   figures show results acquired with protocol-1 (i.e. isotropic voxels).

198

199   **2.4. Data analysis:**

200   A summarized pipeline of our pre-processing methods can be found in **Fig. S1**. Briefly, cortical surfaces were

201   extracted from the anatomical scan following an equi-distance sampling approach and used as a template to map

202   the functional signals using Freesurfer (Martinos Center for Biomedical Imaging, Charlestown, MA). An equi-

203   volume layering sampling was additionally employed (LAYNII, https://github.com/layerfMRI/LAYNII, (Huber

204   et al., 2021b)) to compare the functional results relevant to gyri/sulci (the equi-distance model applies to all

205   figures shown in this report unless specified otherwise). The assessment of the cortical model (results in **Fig.**

206   **S2**) is based on the work by Kay et al. (Kay et al., 2019). Pre-processing included the correction of the magnitude

207   time course to minimize large-vein contribution (**Fig. S3**), as previously described (Menon, 2002, Curtis et al.,

208   2014, Stanley et al., 2021), in conjunction with common pre-processing steps (slice-timing correction,

209   realignment, temporal filtering, and regression of motion parameters as well as averaged white matter and CSF

210   time courses) (Pais-Roldán, 2022), which resulted in zero-mean pre-processed functional time courses. For the

211   assessment of the resting-state measures in task-related scans, the task predictor time course was added as a

212   regressor-of-no-interest so as to avoid interference from an active motor pathway on the assessed metrics (for

213   comparison, the power spectrum and connectivity measures were assessed in all conditions, including the task

214   scan with and without regression of the task paradigm). Post-processing analysis included volume-based ICA-

215   analysis, surface-based temporal correlation (i.e. functional connectivity), surface-based spectral decomposition,

216   amplitude of low-frequency fluctuations (ALFF), surface- and volume-based regional homogeneity (ReHo),

217   and, in task fMRI only, surface-based general linear model (GLM) analysis. Post-processing was performed

218   using 3dRSFC and 3dReHo on AFNI (Analysis of Functional NeuroImages, NIH, Bethesda, MD), Matlab

219   scripts (Mathworks, Natick, MA), and melodic on FSL (FMRIB Software Library, Oxford, UK). The

220   implementation of surface ReHo was based on the functions of the Connectome Computation System ((Xu,

221   2015)). Volume-based analyses (ALFF, volume-based ReHo, and ICA) were followed by a volume-to-surface

222   projection and averaging of vertices within each ROI for a total of 42 ROIs (21 per hemisphere, see **Table 1**)

223   and each surface. Normalization of functional connectivity, ALFF, and ReHo was performed by subtracting the

224   mean value across the brain and dividing by the standard deviation. Computations involving sulcal or gyral

225   locations were restricted to vertices corresponding to the top or bottom 20% curvature values, respectively.

226   Note that the term "surfaces" or "layers" employed through the manuscript should not be interpreted as

227   histologically-defined cortical layers; instead, the terms are employed to refer to each of the six different cortical

228   depths that are artificially generated by splitting the cortical thickness into five different compartments. A more

229   detailed explanation of the methods used to generate the presented results can be found in the *Supplementary*

230   *Material*.

3. RESULTS

3.1. Characterization of the cortical template for whole-brain laminar mapping

In a recent report, we demonstrated the feasibility of using TR-external EPIK to assess fMRI activity over a large FOV with submillimeter spatial resolution (Yun, 2020). The additional acquisition of a structural MP2RAGE sequence enabled us to produce a surface model of the cerebral cortex for each subject. Based on this model, it was possible to study brain activity at six different cortical depths, referred to hereafter as "layers" (different from the cytoarchitectonically-defined cortical layers) and specified as "pial, +80%, +60%, +40% +20%, and white", from the most superficial to the deepest portion of the cortex, respectively. These layers were used as a template for analysis of the functional data (see *Methods* and **Fig. S1**). **Fig. S2** provides a characterization of the cortical model. In **Fig. S2A**, an example of the distribution of sulci and gyri, i.e. the curvature of the cerebral cortex and cortical thickness, is provided for a representative coronal slice. The spatial resolution of each surface was assessed in sulci and gyri independently. As the cortical surfaces were generated by inflating the inner cortical boundary towards the pial space, a one-to-one correspondence between vertices existed across all surfaces; hence, the in-surface resolution varied depending on the depth and the curvature (for a visual example, see insets in **Fig. S2B**). The histograms in **Fig. S2B** show the distribution of vertex-to-vertex distances at different cortical depths for gyri (blue) and sulci (green), in both cerebral hemispheres, as a mean ± standard deviation (SD), obtained from an 18-subject group. In agreement with previous work (Kay et al., 2019), it was observed that, in gyri, the vertex-to-vertex distance increased from 'white' to 'pial'; on average, a sparse distance of 0.72±0.04 mm existed between the vertices in the pial surface, whereas this distance was 0.49±0.01 mm in the white surface, i.e. the surface spatial resolution improved with depth in gyri locations. In contrast, in sulci, the vertex-to-vertex distance decreased from 'white' to 'pial', with an average of 0.36±0.01 mm between consecutive vertices in the pial surface vs. 0.49±0.02 mm between the vertices of the deepest layer, i.e. outer surfaces were more densely sampled in sulci. This feature was observed in both the left and right hemispheres. The upper inset in **Fig. S2B** exemplifies the larger vertex-to-vertex distance in the superficial layers of the cortical gyri, and the inset below exemplifies the larger distance between consecutive vertices in gyri compared to sulci. Cortical thickness was calculated in both cerebral hemispheres for 21 ROIs and for gyri and sulci in the whole cortex (**Fig. S2C**). Note that the analysis specific to gyri or sulci only considered the bottom 20% and top 20% curvature values, respectively (see *Methods*). Given that the cortical ribbon is thicker in the crown of gyri than in their walls or in the fundus of sulci (Kay et al., 2019) (**Fig. S2C**, blue bar vs. green bar), the layer-to-layer separation is greater at this position of the gyri (**Fig. S2D**, 0.62±0.02 mm between layers of cortical gyri vs. 0.40±0.01 mm in sulcal locations), which indicates that higher signal contamination from neighboring layers can be expected in sulci, particularly in their fundus. Note that the in-depth resolution in the crown of gyri, i.e. the inter-layer distance, approximately corresponds to the voxel size employed in our fMRI protocol. The relative differences in surface resolution and inter-layer distance across cortical depths are in broad agreement with the study of Kay et al. (Kay et al., 2019). However, their results showed a slightly better surface resolution,

10

267 which was probably due to having increased the density of surface vertices during processing, a step that was

268 avoided here to limit the computational demands of the whole-cortex functional analysis. **Fig. S4** shows the

269 sampling of the different cortical depths overlaid on the anatomical and the mean functional images for a

270 representative case. The characterization of the cortical surfaces suggested that the chosen subject-specific

271 cortical model could be used as a reliable template to map functional signals and to study layer-based functional

272 oscillations.

273

274 **3.2. De-vein of the high-resolution GE-EPIK**

275 Given the susceptibility of GE images to the signal of ascending venules and pial veins, we adopted the

276 correction method described by Menon et al. (Menon, 2002, Curtis et al., 2014). This method consists of using

277 the information in the phase signal, which is presumably proportional to changes in oxygenated/deoxygenated

278 hemoglobin in non-randomly oriented vessels, to remove unwanted signal change from the magnitude signal.

279 The procedure should, therefore, minimize the contribution of large vessels (mainly in upper cortical layers and

280 veins in the CSF compartment) while preserving the signal of the gray matter capillaries. **Fig. S3** exemplifies

281 the correction method by displaying the average magnitude, phase, and corrected magnitude signal time course

282 in four regions at different cortical depths in the precentral gyrus during task performance (the same method was

283 applied to the resting-state data). The signal from voxels near the CSF ("1" in **Fig. S3C**) is substantially affected

284 by Menon's de-vein procedure, but the change is much less evident in deeper gray matter voxels (e.g., "3", "4"

285 or "5" in **Fig. S3C**). The contribution of large vessels can be reduced by using this correction step.

286

287 **3.3. Depth-dependent evoked responses in the primary motor cortex (M1)**

288 In order to prove the capabilities of TR-external EPIK for use in a laminar analysis of the whole brain, we first

289 aimed to reproduce the results obtained in previous fMRI studies of finger-motor tasks. These results are

290 characterized by a strong response in the upper layers of M1 and a second activation peak in the middle-deep

291 layers when avoiding non-corrected GE-BOLD sequences (Huber et al., 2017, Chai et al., 2020, Huber et al.,

292 2015). A task-based fMRI protocol consisting of 12 epochs, alternating 21 s blocks of finger motion with 21 s

293 blocks of rest, was conducted on each subject using a submillimeter-resolution protocol configured with TR-

294 external EPIK; voxel size: 0.63 mm isotropic, matrix: 336×336, 123 slices (see protocol-1 in *Methods*). In

295 agreement with the previous literature (Huber et al., 2017, Chai et al., 2020, Huber et al., 2015), we observed a

296 marked predominance of the BOLD response in the superficial layers of M1 (**Fig. 1**). A monotonous signal

297 decrease from superficial to deep layers, typical in laminar GE-BOLD, was observed after averaging the beta

298 coefficient within a portion of M1 (**Fig. 1A-B**, N=13), possibly reflecting a bias due to ascending veins and large

299 venous vessels located on the surface (**Fig. S5**) that may remain even after the de-vein procedure. However,

300 when sampling the beta-map of area M1-4A (Geyer et al., 1996) (specifically, along 20 lines, each extending

301 from the CSF and up to the WM), we were able to identify a bimodal response superimposed over this gradient

302 in multiple subjects and through several consecutive slices (see mean line profile in **Fig. 1C** and several

11

303 examples through **Fig. S6**). This laminar activation profile resembled the typical profile of finger motor tasks

304 finely assessed in high-resolution schemes (Huber et al., 2017, Chai et al., 2020, Huber et al., 2015). The

305 specificity of laminar responses was further evaluated in one subject by comparing the activation profiles of two

306 different tasks: movement-only, or movement + touch, i.e. somatomotion, or movement + somatosensation (**Fig.**

307 **1K**). While both tasks resulted in an initial activation peak in the superficial layers, the relatively salient response

308 observed in deeper layers during movement was minimized and shifted towards more superficial layers upon

309 the addition of touch. It is worth noting that the post-hoc correction steps to ameliorate the GE-BOLD signal

310 bias towards pial vessels did not include deconvolution of model signal bias across the cortical ribbon (in order

311 to keep consistent pre-processing across task and resting-state data). Although the pre-processed data are likely

312 to be partially biased towards the surface, these results demonstrate the potential of TR-external EPIK to track

313 laminar changes in the human cortex, even without the application of deconvolution procedures.

314

315   **3.4. Near whole-brain assessment of cortical depth-dependent activity in resting-state fMRI**

316 To investigate whole-brain depth-dependent functional measures and cross-layer interactions between distant

317 cortical areas during rest, we acquired two additional task-negative fMRI scans from each subject, one using

318 protocol-1, with 0.63 mm isotropic voxels, i.e. same as for the task-fMRI, and another using protocol-2, with

319 higher in-plane resolution (0.51×0.51 mm^2) and thicker slices (1.00 mm) to maintain a reasonable SNR level.

320 In order to reduce the dimensionality of our data (6 surfaces $\times \sim 290\,000$ vertices per hemisphere), we first

321 segmented the cerebral cortex into 21 ROIs related to well-known brain networks: default mode, visual, sensory-

322 motor, auditory, executive control, and salience (**Table 1**). Having averaged the vertices within each ROI and

323 each cortical layer in both cerebral hemispheres, we obtained 252 time courses from each fMRI scan (21 ROIs

324 $\times$ six surfaces $\times$ two hemispheres). These were then subjected to several analysis methods. Following a

325 frequency-power decomposition of the functional time courses, it was found that most cortical areas exhibit a

326 higher level of activity in their superficial layers (**Fig. 2A**). This activity was observed to oscillate mostly within

327 the range 0.01-0.03 Hz, which is in agreement with other non-laminar rs-fMRI studies focusing on cortical gray

328 matter (Zuo et al., 2010, Xue et al., 2014, Yuen et al., 2019, Bajaj et al., 2014). Integration of the signals

329 fluctuating between 0.01 and 0.1 Hz, i.e. the typical range considered in rs-fMRI studies (Murphy et al., 2013),

330 provided a simplified measure of brain activity during rest, commonly denoted as ALFF, which was assessed

331 for each ROI and the six different cortical depths. **Fig. S7** shows the averaged ALFF (across all ROIs and

332 subjects) for each cortical depth, considering either the whole surface, only gyral locations, or only sulcal

333 locations, and using either the data sampled with an equi-distance or an equi-volume sampling model. ALFF

334 laminar profiles were generated for each ROI. To reduce dimensionality, a linear fitting of the laminar profile

335 was computed, and the slope of the fitting line was calculated and reported per ROI (color-coded in **Fig. 2B**)

336 and per network (**Fig. 2C**, see network color-coding in **Fig. 2D**)). The level of activity (ALFF) was observed to

337 decrease from the surface of the cortex towards the deep gray matter in most ROIs (i.e. negative slope, hot colors

338 in **Fig. 2B**), irrespective of whether these were assessed in cortical gyri or cortical sulci (**Fig. S7**). The sensory-

339   motor network and the auditory network exhibited the most and the least steep ALFF laminar profiles,

340   respectively, in both cerebral hemispheres (red and purple markers in **Fig. 2C**).

341

342   The assessment of layer-specific regional homogeneity (ReHo) demonstrated a more varied distribution (e.g.,

343   positive or negative slopes across ROIs), with a mean negative slope when considering the whole cerebrum (**Fig.**

344   **S8**). **Fig. 2G** shows the ReHo map (mapped from surface to volume space) for a representative subject. The

345   assessment of ReHo through gyri or sulci was conditioned by the model used to sample the layers along the

346   cortical depth. An equi-distant layering resulted in curvature-specific differences, with a positive ReHo slope in

347   most gyral locations (higher ReHo values in deep layers) and a steep negative slope in sulci (higher ReHo in

348   superficial layers), both during rest and task (**Fig. S8A-B**). It is worth considering that, although large veins are

349   more likely to traverse the outer portion of the brain (i.e. gyral locations), the presence of small venules over the

350   sulcal surfaces could contaminate a larger number of nearby brain vertices, yielding higher homogeneity

351   measures among superficial sulcal vertices. However, the differences in the ReHo slope between gyral and sulcal

352   locations were not reproduced using an equi-volume sampling (**Fig. S8D-E**). The equi-volume sampling takes

353   into account that the actual cortical folding leads to thicker superficial and thinner deeper laminae in sulci (and

354   vice-versa in gyri). The heterogeneity of gyri/sulci ReHo results indicates that curvature-relevant assessments

355   should be interpreted with caution and that the employed layer sampling model should be considered in this

356   regard.

357

358   In addition to using ALFF and ReHo to assess brain activity, we investigated the functional connections between

359   different brain regions at different depths of the cerebral cortex. To assess the reliability of our methods, we first

360   conducted a layer-to-layer analysis within the visual system, following Polimeni et al (Polimeni, 2010). Briefly,

361   we computed the temporal correlation, i.e. a proxy of functional connectivity, between the mean time courses

362   of six different depths in the primary visual cortex (V1) of the right and left hemispheres, as well as between

363   these and the layers in the secondary visual cortex (V2). In agreement with the literature (Polimeni, 2010), we

364   observed that the superficial layers of V1 are strongly connected to other superficial layers of the contralateral

365   V1, and that the superficial-intermediate layers of V1 connect mostly to intermediate-deep layers of the

366   ipsilateral V2, probably reflecting a feedforward projection (**Fig. S9**). Next, we conducted a whole-brain

367   functional connectivity analysis. This was done by generating a functional connectivity matrix from each fMRI

368   scan, which included the temporal correlation between all pairs of time courses, i.e. between the average time

369   course of each region at each layer and that of every other region and layer (i.e. 252^2 cells). The correlation

370   values of the six layers in each ROI and the six layers of every other ROI were computed. For group analysis,

371   the connectivity matrices of 13 subjects were averaged and subjected to a t-test for statistical thresholding. The

372   resulting adjacency matrix was then used to generate a layer-specific, whole-brain connectivity graph. A whole-

373   brain connectivity map was computed for each of the three scans acquired per subject, and the results are shown

374   in **Fig. S10I-L**. To facilitate the visual inspection of the depth-dependent connectivity graphs, the six assessed

13

375   layers were grouped into "deep," "intermediate," and "superficial" layers, and connections were color-coded
376   based on the pair of cortical depths involved, e.g., deep–deep connections were represented by yellow lines,
377   intermediate–intermediate connections by red lines, deep-intermediate connections by orange lines, etc. In order
378   to simplify the connectivity results, inter-regional connections were grouped per network. **Fig. 3A-D** shows four
379   versions of four network connectivity graphs, with variable layer visibility, demonstrating the depth-specific
380   significant connections within the DMN, the executive control network, the sensory-motor network, and the
381   visual network, obtained from a resting-state scan acquired with protocol-1 (N=13). The same graphs were also
382   computed from the task-based fMRI obtained with protocol-1 and the rs-fMRI obtained with protocol-2, which
383   can be found in **Fig. S11**. A connectivity analysis based on coherence instead of temporal correlation rendered
384   similar results (**Fig. S12**). The assessment of the cortical depth-dependent connectivity for each functional
385   network, i.e. the average temporal correlation between ROIs of the network at each cortical depth, indicates that
386   the superficial and upper-intermediate layers govern most resting-state correlations within the DMN and the
387   visual network (bell shapes with a peak on the left in **Fig. 3F** –mean depth-dependent network connectivity
388   across subjects (after transforming subject-specific measures to z-scores)-). The intermediate layers are seen to
389   be strongly connected within the sensory-motor network (symmetric profile with a peak in the center in **Fig.
390   3F**), and it is the deep-intermediate portion of the cortex that exhibits the strongest connectivity within the
391   executive control network (peak towards the right in **Fig. 3F**). The shift in laminar connectivity preference
392   towards the infragranular layers in the executive control network was evidenced, for instance, as stronger
393   interhemispheric connections between intermediate layers of the middle frontal gyrus compared to its superficial
394   layers (significant connections in yellow and orange but not blue, between some ROIs in **Fig. 3**: "Executive
395   control"). The laminar connectivity profile of each network computed for all subjects is presented in **Fig. 3E**
396   (before z-score normalization). From a global-ROI perspective, i.e. independent of cortical depth, our data
397   presented multiple significant connections that were in agreement with the volume-based resting-state network
398   results derived from an ICA analysis; volume-based examples and the corresponding depth-dependent profiles
399   per ROI are shown in **Fig. S13**.
400   The identification of stronger connections involving the supragranular layers of the cortex in areas of the DMN
401   is in agreement with previous reports demonstrating a higher level of activity and communication near the
402   surface of the cortex in humans and non-human primates during rest (Guidi et al., 2020, Mishra et al., 2019).
403
404   **3.5. State-dependent cortical-depth specificity of whole-brain functional measures**
405   Having acquired whole-brain scans with high spatial specificity during rest and task performance, we aimed to
406   assess the potential differences between both behavioral states at a laminar level. The slope or gradient of ALFF
407   and ReHo measures along the cortical thickness, i.e. the difference between superficial and deep layers in terms
408   of their signal amplitude and regional homogeneity, was significantly reduced when subjects were engaged in a
409   motor task (**Fig. 4A** and **Fig. 4B**), suggesting that the superficial layers of the cortex are a major factor in the
410   maintenance of resting-state activity that is significantly dampened during task performance. **Fig. S7C,F** and

14

411   **Fig. S8C,F** show the differences in ALFF and ReHo laminar slopes, respectively, between resting-state and task

412   using either an equi-distance or an equi-volume layering approach. In most cases, irespective of the sampling

413   model, the laminar slopes were significantly higher during rest compared to task (i.e. higher ALFF and ReHo in

414   the superficial layers).

415

416   Compared to task fMRI, resting-state scans generally exhibited higher connectivity between remote regions and

417   their layers, as observed in their corresponding whole-brain connectivity graphs in **Fig. S10I-L** and in the

418   network-specific graphs of **Fig. S11**. During the motor task, the connectivity within the executive control

419   network seemed to involve more superficial layers of the cortex compared to rest (note the peak shift towards

420   the left in the blue trace of **Fig. S10G or Fig. S10H** –with or without regression of the task paradigm- compared

421   to **S10E**)). In contrast, more intermediate layers were involved in DMN connectivity during task performance

422   (yellow trace in **Fig. S10G or Fig. S10H** compared to **Fig. S10E,** and **Fig. 4C**). This was observed, for instance,

423   as a stronger correlation between the anterior cingulate cortices of both cerebral hemispheres and a reduced

424   interhemispheric connection of superior temporal and posterior mid-cingulate areas (**Fig. S11A**, middle graph,

425   compared to the left graph).

15

4. DISCUSSION

The layer-specific communication patterns across distant brain regions of the human brain have remained largely unexplored, mainly due to the limited brain coverage afforded by most high-resolution methods. In this report, we employed a recently developed fMRI sequence (TR-external EPIK) to address the question of how the different depths of the cerebral cortex participate in the maintenance of the resting state in humans. We first obtained motor-evoked responses that reproduced the laminar results seen in the existing literature and then provided a cortical-depth specific characterization of resting-state activity spanning multiple brain regions. Our ALFF showed a near-linear trend peaking at the surface of the cortex, likely reflecting vein-related bias, the slope of which was significantly reduced when subjects were engaged in a motor task. The slope of the mean ReHo across layers was also reduced during task performance, and network analysis showed certain differences both between networks and between conditions in terms of the cortical depth at which the connectivity was strongest, e.g., the DMN connectivity peaked at deeper layers in scans acquired during task performance. We interpreted the differences between resting-state data and task data as an indication that functional laminar dynamics can change with the brain state. Although our data may be partially contaminated by the influence of large veins (typical of GE sequences), certain metrics, especially those based on connectivity measures, demonstrated the sensitivity of the sequence to laminar events. Our results suggest that functional connections relevant to particular systems are cortical-depth specific, e.g., we found that intermediate and superficial cortical depths maintain key connectivity patterns in humans (e.g., DMN), in agreement with animal studies (Weiler et al., 2008, Whitesell et al., 2021), but we also identified a laminar connectivity shift towards deeper cortical layers in particular networks (e.g., executive control network).

In this study, we acquired two sets of rs-fMRI data for each subject within the same imaging session: one using isotropic voxels and the other using higher in-plane spatial resolution but with thicker slices. Both sets of data had voxels of similar volume (~ 0.25 mm³). The resemblance between all functional measures assessed in both sets of the rs-fMRI data (**Fig. S10** and **Fig. S11**) suggests that both protocols were able to detect brain connectivity with layer-specificity to a similar level of performance. Given the agreement between both protocols, and since protocol-2 confers a more complete brain coverage, despite the non-isotropic voxel dimensions in protocol-2 ($0.51 \times 0.51 \times 1.00$ mm), it may be a better candidate than protocol-1 for whole-brain laminar fMRI, especially in applications where structures that are located at the base of the brain, e.g., hippocampus, brainstem, etc., are significant for the integrity of the study, as long as the high-resolution plane matches the right dimension in the target area. A more detailed technical description of both of the TR-external EPIK protocols can be found in reference (Yun et al., 2022, Yun, 2022).

In previous literature, higher activation of superficial, i.e. supragranular, cortical layers has been observed in laminar rs-fMRI studies that have focused on a restricted FOV in the human brain (Guidi et al., 2020), in non-

462   human primates (Mishra et al., 2019), and in rodents (Weiler et al., 2008). In contrast to the granular layer,
463   which receives thalamo-cortical afferents, and the deeper, i.e. infragranular, layers, which mainly initiate
464   efferent responses through subcortical and spinal projections, the superficial layers are the principal source and
465   target of cortico-cortical regulatory communication (Moerel et al., 2019, D'Souza and Burkhalter, 2017, Rubio-
466   Garrido et al., 2009, Larkum, 2013, Sempere-Ferrandez et al., 2019, Rolls and Mills, 2017). Hereby, the deeper
467   portion of layer III receives long-distance feedforward projections, whereas its superficial portion, together with
468   layer II, is targeted by long-distance feedback projections (Zilles and Catani, 2020). The present results support
469   the supposition that superficial layers play a role in resting-state maintenance, as resting-state networks mostly
470   involve cortical areas (Raichle et al., 2001, Heine et al., 2012); however, our results also demonstrate a network-
471   specific laminar connectivity profile, i.e. not all networks' connectivity peaked in intermediate/superficial
472   territories. For instance, the connectivity within the sensory-motor network was stronger in the intermediate
473   layers, which is consistent with feedforward connections from the thalamus to the sensory areas (e.g., postcentral
474   gyrus), while higher-order networks, such as the DMN or the executive control network, mostly involved
475   superficial or deep connections, suggesting feedback processing. However, it is worth noting that although
476   directionality has been well studied within some sensory systems, e.g., in the visual pathway, the laminar
477   preference of feedforward and feedback projections in other brain areas, and especially at the network level, is
478   less well understood (for a review, see reference (Rockland, 2019)); hence, interpretations in this regard should
479   be made with caution.

480

481   Although the literature upholds the results obtained from our resting-state analysis, i.e. strong participation of
482   the superficial layers during rest (here observed with ALFF, ReHo, and connectivity measured within the DMN)
483   or particular connectivity patterns in the visual system (e.g., feedforward connections between V1 and V2), the
484   GE nature of the sequence employed poses the question as to whether the recorded signal could be merely a
485   reflection of a vascular-related superficial bias, potentially further enhanced by a higher SNR near the surface
486   of the brain (i.e. stronger T2 signal near the CSF). While the amplitude of the fMRI signal was generally higher
487   in the superficial layers (measured as ALFF during rest and also indicated by the larger evoked responses on the
488   superficial layers during task performance), likely partially due to the higher signal produced in superficial
489   vascular territories, the varied connectivity results shown here demonstrate that the ability of the fMRI sequence
490   to map depth-specific connections was not compromised to the extent of masking interactions occurring below
491   the surface of the cortex. In fact, the connectivity measures rarely peaked on the most external layer of the
492   cortex, and in some cases, the highest connectivity values were found in deeper territories; our results showed a
493   network-dependent behavior of laminar connectivity. Besides, the fact that the layer-dependent signal amplitude,
494   regional homogeneity, and whole-brain connectivity were significantly altered upon task performance using
495   exactly the same imaging protocol (**Fig. 4**, **Fig. S10**, **Fig. S11**) suggests that a vein-related bias, if present, was
496   not the only factor accounting for the observed responses. Notwithstanding this assertion, the potential
497   implications of using a GE-based sequence will be discussed in a later paragraph.

17

498

499 The analysis of ALFF and ReHo in cortical regions of marked curvature (20% top and bottom curvature values,
500 i.e. sulci or gyri) was conducted on six cortical surfaces extracted through equi-distant sampling and on six
501 cortical territories segmented based on an equi-volume model. While both approaches provided similar results
502 at a whole-brain level, gyri and sulci were characterized by different ReHo laminar profiles depending on the
503 employed sampling method; in particular, the differences encountered when using the equi-distant sampling
504 practically vanished with the equi-volume approach. This is probably due to the fact that the actual folding of
505 cortical laminae leads to thicker superficial laminae in sulci vs. gyri (Bok, 1929), which is reproduced with an
506 equi-volume but not with an equi-distant sampling (Waehnert et al., 2014). However, it is worth adding that our
507 analysis based on equi-distance sampling was performed on surface-space, i.e. ReHo was conducted within each
508 surface, while the ReHo results from equi-volume-based were obtained in voxel space first and later mapped to
509 each territory in the segmented cortical ribbon. The latter approach is likely to be influenced by voxels from
510 neighboring depths. In any case, our results suggest that, while depth-dependent levels of homogeneity evaluated
511 in the gross cortex are similarly informed by both sampling approaches, and hence seem robust, finer differences
512 pertaining to ReHo in sulci and gyri should be interpreted with caution.

513

514 In comparison to the resting-state paradigm, the assessment of layer-specific correlations during task
515 performance revealed a decreased number of functional connections (**Fig. S10K** vs. **Fig. S10I**), which is in
516 agreement with the literature (Jurkiewicz et al., 2018). The specificity of the responses evoked by the motor task
517 was demonstrated with distinct line profiles in the precentral gyrus, in response to somatomotion, with and
518 without somatosensation (**Fig. 1K**). Finger movement resulted in activation of the superficial and, to a lesser
519 extent, deeper layers, the latter possibly indicating signaling from premotor and supplementary motor cortices,
520 also coinciding with cortical motor efferents towards pontomedullary or thalamic nuclei (Weiler et al., 2008,
521 Hooks et al., 2013). Sensory processing triggered by the touch between two fingers produced activation in
522 intermediate layers, possibly reflecting the modulation of the motor cortex by sensory cortical areas and afferents
523 from the sensory thalamus (Weiler et al., 2008, Hooks et al., 2013, Mao et al., 2011). The activation observed
524 near the cortical surface may reflect, at least to a certain extent, a contribution from the venous network;
525 however, our laminar profiles do not merely present a linear vein bias. Moreover, superficial neuronal responses
526 can be expected during the performance of a motor task, as motor thalamic afferents modulate motor behavior
527 in the superficial and intermediate layers of the cortex in a similar way to the sensory thalamic afferents upon
528 the addition of touch (Hooks et al., 2013) - which has also been observed in laminar studies (Huber et al., 2017).
529 The fact that evoked responses in the intermediate and deep layers were detected in a line-profile analysis but
530 not in the analysis of a bigger cortical patch, also responding to the motor task but exhibiting an upper → deeper
531 trend only, demonstrates the specificity of the laminar responses on particular cortical regions and the overall
532 preponderance of BOLD responses in the superficial layers in less specific evaluations. Although some
533 corrections could be applied to the evoked responses to compensate for the vasculature-related gradient, we

18

534   deferred from using this procedure. This was done to avoid masking the contribution of non-neuronal sources

535   that would be present in the resting state data, i.e. we opted for applying the same correction to task and resting-

536   state data, as correction of the latter using existing models is currently not straightforward.

537

538   It could be argued that, aside from the potential venous influence, the higher SNR in the superficial layers (e.g.,

539   **Fig. 1E**, upper layers showing higher mean MR signal in the TR-external EPIK image) could facilitate the

540   detection of functional responses and connections between superficial cortical depths. However, as superficial,

541   intermediate, and deep connections pertaining to different network systems were detected differently during task

542   performance and during rest (e.g., **Fig. 4C**, **Fig. S10**, **Fig. S11**), and the ALFF and ReHo laminar gradients were

543   reduced during task performance (**Fig. 4A-B**), it is likely that functional information remains in the high-

544   resolution data, despite potential bias in favor of the superficial layers; i.e. not all activations and connections

545   were observed in the most external layer of the cortex or to the same extent, independent of the behavioral

546   condition. The evaluation of typical resting-state measures in our task-fMRI scans after regression of model

547   activation responses provided a reference framework of potential changes at the level of cortical laminae relevant

548   to the brain state. Although most connections that are typically found during the resting state exist in task-related

549   data, our results showed that the preferred layers to maintain such connections can change, e.g., the DMN during

550   task appears less supported by superficial layers than during rest (**Fig. 4C**, **Fig. S10G vs. Fig. S10E** and **Fig.

551   S11A**). It is well known that the connectivity of the DMN decreases during task performance (Raichle et al.,

552   2001), which is consistent with the obtained results and may also explain the shift from superficial to

553   intermediate layers (possibly reflecting reduced feedback processing during task performance); however, a

554   decrease of activity in DMN areas is also expected to be bound to a reduced blood flow and, hence, to a potential

555   improvement (reduction) of the superficial bias, which should be taken into consideration when interpreting the

556   task-related whole-brain results.

557

558   The selected fMRI sequence integrates a number of acceleration techniques that enable a large matrix with fine

559   resolution to be sampled without compromising the quality of the data (the sequence implementation has been

560   previously demonstrated in comparison to EPI (Yun and Shah, 2017, Yun et al., 2013)). In TR-external EPIK,

561   the high spatial resolution is partially possible due to the segmented sampling of the k-space periphery. While

562   full k-space sampling is completed every 3 TRs, the combination of this with a fully sampled center k-space at

563   each TR confers upon TR-external EPIK enough temporal resolution to sample brain hemodynamics with sub-

564   millimeter resolution ((Yun et al., 2019, Yun and Shah, 2017, Yun et al., 2013, Yun and Shah, 2019, Yun, 2022)).

565   The results from the group of subjects studied in this work demonstrate the feasibility of using TR-external EPIK

566   for the detection of layer-specific functional signals. In our protocol, the sharing of missing k-space lines is

567   limited to the adjacent two scans, the energy of which was determined to be smaller than 10% of the entire k-

568   space energy. Although the peripheral k-space is updated slowly (i.e. 3 TRs = 10.5 s; ~0.1 Hz), it is sufficient to

569   track the change of resting-state signals, the peaks of which are usually detected within a frequency of 0.03-0.04

19

570　　Hz (Zuo et al., 2010, Xue et al., 2014, Yuen et al., 2019, Bajaj et al., 2014) in the gray matter. Furthermore, it

571　　has been reported that conventional resting-state analyses are not significantly altered by TR (Huotari et al.,

572　　2019), and methods employing relatively slow sampling have succeeded in tracking laminar dynamics (e.g.,

573　　3960ms (Sharoh et al., 2019), 5000ms (Barry et al., 2021), 8300ms (Huber et al., 2020)). Despite the advantages

574　　of TR-external EPIK over conventional EPI, the GE nature of the technique makes it susceptible to vein-derived

575　　contamination, just as any other GE-EPI sequence. Assuming a fair neuro-vascular coupling, the fMRI signal

576　　extracted from a cortical capillary network is a reliable indicator of neuronal activity. However, capillaries

577　　supplying blood to neurons flow in bigger ascending venules that run perpendicular to the cortex and disgorge

578　　into pial veins tangential to the surface of the brain, and these veins influence the fMRI signal and can result in

579　　a bias towards the superficial layers of the cortex. This bias is reduced in other acquisition schemes, such as SE-

580　　BOLD fMRI, sensitive to oxygenation changes in the microvasculature only, vascular space occupancy fMRI

581　　(VASO), sensitive to vessel dilation, or cerebral blood flow-based fMRI (CBF), sensitive to flow changes. Due

582　　to the short T2 constant of blood at ultra-high field, BOLD-fMRI at 7T is only sensitive to the extra-vascular

583　　effect of the oxy/deoxy-hemoglobin ratio, irrespective of vessels size. Although the parenchymal vessels, i.e.

584　　venules of diameter < 25 μm, are detected by both SE- and GE-BOLD, these are often overshadowed in GE

585　　sequences by the influence of bigger veins running along the surface of the brain, which cause static

586　　perturbations in the magnetic field affecting the neighboring parenchymal tissue. Therefore, while SE-BOLD

587　　offers a fine localization of the activated parenchyma, GE-BOLD provides a mixed signal that is relevant to both

588　　small parenchymal vessels and macroscopic veins. To correct for this bias, we subtracted the time-varying phase

589　　component of the MR signal from each voxel's magnitude time course. The time-varying phase component is

590　　proportional to the frequency offset exhibited by the spins and hence, sensitive to the venous vasculature

591　　(Menon, 2002, Curtis et al., 2014). As large vessels produce field inhomogeneities, spins processing in the

592　　neighboring parenchyma would produce changes in the phase component of the signal; in contrast, small

593　　randomly oriented vessels, e.g., in the capillary network within the gray matter, do not produce a net phase and

594　　hence, their derived signal remains intact. Although this method helps to improve the local specificity of BOLD,

595　　several biases could remain in the corrected data, such as those derived from motion correction or geometric

596　　distortions (Bause et al., 2019), which reduce the ultimate spatial resolution of GE sequences. However, it is

597　　worth noting that geometric distortions are less pronounced in EPIK compared to conventional EPI, and in fact,

598　　the PSF of GE-EPIK is narrower than in conventional GE-EPI (Yun et al., 2013). A few groups have

599　　demonstrated the dependence of laminar fMRI on the orientation of the cortex with respect to B0 (Viessmann

600　　et al., 2019, Baez-Yanez et al., 2017). Although orientation bias can be critical for the dissection of the fMRI

601　　signal, this effect has been correlated with low-frequency drift, motion, and respiratory cycles, which were

602　　accounted for in our study, therefore diminishing the discussed effect. Moreover, most of our results were

603　　obtained from relatively big patches of the cortex and through multiple ROIs, averaging vertices with different

604　　orientations within a cortical surface. Hence, although non-negligible, an orientation bias is not expected to have

605   conditioned our results. However, a future model accounting for such an effect could determine the extent to

606   which the curvature affects the laminar profiles at a whole-brain level.

607

608   Although the 2D acquisition scheme employed in our TR-external EPIK sequence could raise concerns relating

609   to the increased susceptibility to inflow effects compared to 3D-EPI, this increased susceptibility is only

610   significant when a relatively short TR (i.e. tens of a millisecond) is used (Frahm et al., 1994). Hence, signal

611   changes induced by the inflow effect are negligible in most 2D multi-slice fMRI protocols configured with a TR

612   larger than 1.5 s (Speck and Hennig, 1998, Howseman et al., 1999, Wiggins, 2000, Gao and Liu, 2012). Since

613   our protocol also uses a relatively long TR (3.5 s), the inflow effect on the detection of the fMRI signal can be

614   considered insignificant. In EPIK, the multi-shot scheme for the peripheral k-space can lead to an increased

615   sensitivity to the subject motion when compared to EPI. However, the sampling of the central k-space region at

616   every temporal scan in EPIK can effectively ensure comparable temporal stability to the EPI case, enabling a

617   robust acquisition of fMRI time-series data (Yun and Shah, 2017, Yun et al., 2013). As 3D EPI often requires

618   additional correction methods to account for intra-scan motion artifacts, 2D EPIK can be more straightforwardly

619   deployed in an fMRI study.

620

621   In contrast to retrospective model-based approaches that reduce the superficial BOLD bias by applying temporal

622   decomposition (Kay et al., 2020), linear detrending (Fracasso et al., 2018), normalization (Kashyap et al.,

623   2018a), or deconvolution (Heinzle et al., 2016, Markuerkiaga et al., 2016) to evoked fMRI data, the phase-based

624   correction method employed here does not involve a priori assumptions about the behavior of the vascular

625   dynamics across the cortical thickness and does not rely on the use of an evoked paradigm, offering a bias-free

626   alternative to correct resting-state GE-fMRI data. Based on our results, this phase-based method (Menon, 2002)

627   may constitute a rather conservative approach, i.e. the activity of the superficial layers was found to predominate

628   almost ubiquitously (higher ALFF in upper layers of the cortex). However, connectivity analysis did identify

629   laminar interactions in a cortical profile different from the linear gradient that would be expected in purely

630   macro-vascular measures, i.e. with a maximum on the surface, and the evoked responses were composed of two

631   peaks, the latter located in deeper layers of the cortex, indicating a decent laminar sensitivity. Future studies

632   employing GE TR-external EPIK and SE TR-external EPIK in a combined acquisition will investigate the

633   possibility of complementing the phase-correction method with additional strategies to exploit the high SNR of

634   GE schemes with robust laminar specificity.

635

636   The vascular dependence of the fMRI signal remains one of the biggest challenges in laminar fMRI (Uludag

637   and Blinder, 2018). Signals obtained with BOLD contrast are not only conditioned by a physically-constrained

638   laminar point-spread function, i.e. the fact that ascending venules spread the deep activation signals towards

639   superficial layers (Havlicek and Uludag, 2020, Markuerkiaga et al., 2016, Marquardt et al., 2018), but also by

640   the varying physiological mechanisms underlying the BOLD response (CBF, CMRO2, CBV), which can

21

641   modulate this point-spread function across cortical layers (Havlicek and Uludag, 2020). Despite the complexity

642   of the model, laminar fMRI studies have even employed strategies that artificially sample the cortical depth with

643   a number of points higher than the number of voxels across the cortical ribbon. This is appropriate under the

644   assumption that the purpose of the study is to track the trend of activation across the cortical depth and not to

645   resolve the actual neuronal signal at any particular layer, which is indeed not possible, even with sufficient

646   spatial resolution, given the facts discussed above. In this study, the number of depths used was equal to the

647   number of histologically-defined layers in the neocortex; however, the layers in our model have been arbitrarily

648   chosen to be equally spaced along the cortical thickness and have no direct relationship with the cortical

649   cytoarchitecture. Hence, our conclusions should be interpreted in terms of cortical depth only. Although some

650   reports have chosen a smaller number of layers for their laminar assessment, e.g., three (Sharoh et al., 2019),

651   which simplifies the analysis and confers layers with a greater independence, others have shown that a greater

652   number of depths, e.g., twenty (Huber et al., 2017), enables clearer detection of cortical responses, despite the

653   fact that this strategy involves a greater dependence on neighbor signals. In addition, the latter scheme also poses

654   an important challenge in whole-brain studies due to the high computational demands of the analysis procedure

655   (see discussion below).

656

657   Irrespective of the number of layers, ambitious whole-brain laminar fMRI studies should ensure perfect co-

658   registration between the anatomical reference scan and the functional data. Previous reports have shown the

659   possibility of integrating T1 contrast within a high-resolution fMRI sequence (e.g., (Huber et al., 2017), acquired

660   during VASO), which allows a 1:1 relationship between the anatomical and functional scans, mitigating any co-

661   registration concern. This option was not yet available in the current study. Nevertheless, in this work, we

662   achieved acceptable co-registration in the majority of the brain by using manual rigid transformations (**Fig. S14**),

663   which proved to be more reliable than the transformations rendered by non-linear automatic registration tools.

664   In addition, the improved robustness against geometric distortions in TR-external EPIK (Yun et al., 2013) is

665   expected to yield fewer co-registration errors, compared to the common EPI, between the functional scans and

666   the anatomical scans (e.g., MR2RAGE). However, particular areas in different subjects remained poorly co-

667   registered and needed to be masked out to ensure accurate laminar analysis. In the future, TR-external EPIK will

668   be modified to provide a T1 contrast, which will avoid data loss, reduce the pre-processing time, and, more

669   importantly, will alleviate the potential concerns relating to co-registration.

670

671   In this work, we employed TR-external EPIK to map the majority of the brain with a voxel resolution of $0.63 \times$

672   0.63×0.63 mm^3 or $0.51 \times 0.51 \times 1.00$ mm^3. In addition to the challenge in terms of sequence design, the

673   resulting matrix size imaged by TR-external EPIK ($336 \times 336 \times 123$ or $408 \times 408 \times 108$) presents important

674   computational limitations in post-processing, such as the relatively large memory required (minimum storage

675   space: ~ 6 Gb per 4D-volume; RAM: $\geq$ 32Gb for many pre-processing steps) and long processing times. After

676   pre-processing, analysis of the cortical surfaces with numerical computing environments such as Matlab is,

22

677   again, conditioned by the number of vertices to be processed. Therefore, the greater the number of layers, the

678   higher the computational demands. For instance, one cortical surface covered by protocol-1 contained ~ 290,000

679   vertices, which means that the six surfaces obtained from both hemispheres involved the analysis of ~ 3,480,000

680   vertices, each of them consisting of a 168-point time course. In this work, in order to adjust the computational

681   demands to those of a standard scientific workstation, the first step in most of the layer-specific functional

682   analyses was to average all vertices specific to one layer within one ROI. Given that the laminar performance

683   of the cortex can be highly localized, some events might be overlooked when using an ROI-based analysis to

684   identify particular behaviors; hence, the use of supercomputing resources to assess vertex-specific measures

685   becomes highly desirable to exploit the information contained in the acquired data.

686

687   This study adopted a sequence offering high spatial resolution (~ 0.25 mm^3 voxels) to map laminar functional

688   dynamics in a 7T scanner with near whole-brain mapping in healthy subjects. We investigated the dependence

689   of common rs-fMRI measures such as ALFF, ReHo, and functional connectivity on cortical depth, which has

690   emerged as a new dimension to be explored in the human brain. Our results indicate that the cortical depth is

691   differentially (functionally) connected depending on the resting-state network, with intermediate and superficial

692   layers playing a critical role in the maintenance of the DMN, and further show that the laminar involvement can

693   change during a motor task. This work demonstrates the potential of laminar analysis of connectivity in the study

694   of broad cortical networks, which may have direct implications in the research of psychiatric disorders that are

695   commonly associated with network disturbances.

References:

Adesnik, H. and Naka, A. (2018) 'Cracking the Function of Layers in the Sensory Cortex', *Neuron,* 100(5), pp. 1028-1043. doi: 10.1016/j.neuron.2018.10.032

Ayaz, A., Stauble, A., Hamada, M., Wulf, M. A., Saleem, A. B. and Helmchen, F. (2019) 'Layer-specific integration of locomotion and sensory information in mouse barrel cortex', *Nat Commun,* 10(1), pp. 2585. doi: 10.1038/s41467-019-10564-8

Baez-Yanez, M. G., Ehses, P., Mirkes, C., Tsai, P. S., Kleinfeld, D. and Scheffler, K. (2017) 'The impact of vessel size, orientation and intravascular contribution on the neurovascular fingerprint of BOLD bSSFP fMRI', *Neuroimage,* 163, pp. 13-23. doi: 10.1016/j.neuroimage.2017.09.015

Bajaj, S., Drake, D., Butler, A. J. and Dhamala, M. (2014) 'Oscillatory motor network activity during rest and movement: an fNIRS study', *Front Syst Neurosci,* 8, pp. 13. doi: 10.3389/fnsys.2014.00013

Barry, R. L., Babu, S., Anteraper, S. A., Triantafyllou, C., Keil, B., Rowe, O. E., Rangaprakash, D., Paganoni, S., Lawson, R., Dheel, C., Cernasov, P. M., Rosen, B. R., Ratai, E. M. and Atassi, N. (2021) 'Ultra-high field (7T) functional magnetic resonance imaging in amyotrophic lateral sclerosis: a pilot study', *Neuroimage Clin,* 30, pp. 102648. doi: 10.1016/j.nicl.2021.102648

Bause, J., Polimeni, J. R., Stelzer, J., In, M. H., Ehses, P., Kraemer-Fernandez, P., Aghaeifar, A., Lacosse, E., Pohmann, R. and Scheffler, K. (2019) 'Impact of prospective motion correction, distortion correction methods and large vein bias on the spatial accuracy of cortical laminar fMRI at 9.4 Tesla', *Neuroimage,* 208, pp. 116434. doi: 10.1016/j.neuroimage.2019.116434

Bok, S. T. (1929) 'Der Einfluss der in den Furchen und Windunden auftretenden Kruemmungen der Grosshirnrinde auf die Rindenarchitektur', *Zeitschrift fuer die gesamte Neruologie und Psychiatrie,* 121(682). doi: https://doi.org/10.007/BF02864437

Caldeira, L. L., Yun, S. D., da Silva, N. A., Filss, C. and Shah, N. J. (2019) 'Dynamic susceptibility contrast parametric imaging using accelerated dual-contrast echo planar imaging with keyhole', *J Magn Reson Imaging,* 50(2), pp. 628-640. doi: 10.1002/jmri.26639

Chai, Y., Li, L., Huber, L., Poser, B. A. and Bandettini, P. A. (2020) 'Integrated VASO and perfusion contrast: A new tool for laminar functional MRI', *Neuroimage,* 207, pp. 116358. doi: 10.1016/j.neuroimage.2019.116358

Csercsa, R., Dombovari, B., Fabo, D., Wittner, L., Eross, L., Entz, L., Solyom, A., Rasonyi, G., Szucs, A., Kelemen, A., Jakus, R., Juhos, V., Grand, L., Magony, A., Halasz, P., Freund, T. F., Magloczky, Z., Cash, S. S., Papp, L., Karmos, G., Halgren, E. and Ulbert, I. (2010) 'Laminar analysis of slow wave activity in humans', *Brain,* 133(9), pp. 2814-29. doi: 10.1093/brain/awq169

Curtis, A. T., Hutchison, R. M. and Menon, R. S. (2014) 'Phase based venous suppression in resting-state BOLD GE-fMRI', *Neuroimage,* 100, pp. 51-9. doi: 10.1016/j.neuroimage.2014.05.079

D'Souza, R. D. and Burkhalter, A. (2017) 'A Laminar Organization for Selective Cortico-Cortical Communication', *Front Neuroanat,* 11, pp. 71. doi: 10.3389/fnana.2017.00071

De Martino, F., Esposito, F., van de Moortele, P. F., Harel, N., Formisano, E., Goebel, R., Ugurbil, K. and Yacoub, E. (2011) 'Whole brain high-resolution functional imaging at ultra high magnetic fields: an application to the analysis of resting state networks', *Neuroimage,* 57(3), pp. 1031-44. doi: 10.1016/j.neuroimage.2011.05.008

De Martino, F., Moerel, M., Ugurbil, K., Goebel, R., Yacoub, E. and Formisano, E. (2015) 'Frequency preference and attention effects across cortical depths in the human primary auditory cortex', *Proc Natl Acad Sci U S A,* 112(52), pp. 16036-41. doi: 10.1073/pnas.1507552112

742 Fracasso, A., Luijten, P. R., Dumoulin, S. O. and Petridou, N. (2018) 'Laminar imaging of positive and
743   negative BOLD in human visual cortex at 7T', *Neuroimage,* 164, pp. 100-111. doi:
744   10.1016/j.neuroimage.2017.02.038
745 Frahm, J., Merboldt, K. D., Hanicke, W., Kleinschmidt, A. and Boecker, H. (1994) 'Brain or vein--
746   oxygenation or flow? On signal physiology in functional MRI of human brain activation', *NMR*
747   *Biomed,* 7(1-2), pp. 45-53. doi: 10.1002/nbm.1940070108
748 Gao, J. H. and Liu, H. L. (2012) 'Inflow effects on functional MRI', *Neuroimage,* 62(2), pp. 1035-9.
749   doi: 10.1016/j.neuroimage.2011.09.088
750 Geyer, S., Ledberg, A., Schleicher, A., Kinomura, S., Schormann, T., Burgel, U., Klingberg, T.,
751   Larsson, J., Zilles, K. and Roland, P. E. (1996) 'Two different areas within the primary motor
752   cortex of man', *Nature,* 382(6594), pp. 805-7. doi: 10.1038/382805a0
753 Glover, G. H., Li, T. Q. and Ress, D. (2000) 'Image-based method for retrospective correction of
754   physiological motion effects in fMRI: RETROICOR', *Magn Reson Med,* 44(1), pp. 162-7. doi:
755   10.1002/1522-2594(200007)44:1<162::aid-mrm23>3.0.co;2-e
756 Guidi, M., Huber, L., Lampe, L., Gauthier, C. J. and Moller, H. E. (2016) 'Lamina-dependent calibrated
757   BOLD response in human primary motor cortex', *Neuroimage,* 141, pp. 250-261. doi:
758   10.1016/j.neuroimage.2016.06.030
759 Guidi, M., Huber, L., Lampe, L., Merola, A., Ihle, K. and Moller, H. E. (2020) 'Cortical laminar resting-
760   state signal fluctuations scale with the hypercapnic blood oxygenation level-dependent
761   response', *Hum Brain Mapp,* 41(8), pp. 2014-2027. doi: 10.1002/hbm.24926
762 Havlicek, M. and Uludag, K. (2020) 'A dynamical model of the laminar BOLD response', *Neuroimage,*
763   204, pp. 116209. doi: 10.1016/j.neuroimage.2019.116209
764 Heine, L., Soddu, A., Gomez, F., Vanhaudenhuyse, A., Tshibanda, L., Thonnard, M., Charland-Verville,
765   V., Kirsch, M., Laureys, S. and Demertzi, A. (2012) 'Resting state networks and consciousness:
766   alterations of multiple resting state network connectivity in physiological, pharmacological,
767   and pathological consciousness States', *Front Psychol,* 3, pp. 295. doi:
768   10.3389/fpsyg.2012.00295
769 Heinzle, J., Koopmans, P. J., den Ouden, H. E. M., Raman, S. and Stephan, K. E. (2016) 'A
770   hemodynamic model for layered BOLD signals', *Neuroimage,* 125, pp. 556-570. doi:
771   10.1016/j.neuroimage.2015.10.025
772 Hooks, B. M., Mao, T., Gutnisky, D. A., Yamawaki, N., Svoboda, K. and Shepherd, G. M. (2013)
773   'Organization of cortical and thalamic input to pyramidal neurons in mouse motor cortex', *J*
774   *Neurosci,* 33(2), pp. 748-60. doi: 10.1523/JNEUROSCI.4338-12.2013
775 Howseman, A. M., Grootoonk, S., Porter, D. A., Ramdeen, J., Holmes, A. P. and Turner, R. (1999) 'The
776   effect of slice order and thickness on fMRI activation data using multislice echo-planar
777   imaging', *Neuroimage,* 9(4), pp. 363-76. doi: 10.1006/nimg.1998.0418
778 Huber, L., Finn, E. S., Chai, Y., Goebel, R., Stirnberg, R., Stocker, T., Marrett, S., Uludag, K., Kim, S.
779   G., Han, S., Bandettini, P. A. and Poser, B. A. (2020) 'Layer-dependent functional connectivity
780   methods', *Prog Neurobiol*, pp. 101835. doi: 10.1016/j.pneurobio.2020.101835
781 Huber, L., Finn, E. S., Chai, Y., Goebel, R., Stirnberg, R., Stocker, T., Marrett, S., Uludag, K., Kim, S.
782   G., Han, S., Bandettini, P. A. and Poser, B. A. (2021a) 'Layer-dependent functional connectivity
783   methods', *Prog Neurobiol,* 207, pp. 101835. doi: 10.1016/j.pneurobio.2020.101835
784 Huber, L., Goense, J., Kennerley, A. J., Trampel, R., Guidi, M., Reimer, E., Ivanov, D., Neef, N.,
785   Gauthier, C. J., Turner, R. and Moller, H. E. (2015) 'Cortical lamina-dependent blood volume
786   changes in human brain at 7 T', *Neuroimage,* 107, pp. 23-33. doi:
787   10.1016/j.neuroimage.2014.11.046
788 Huber, L., Handwerker, D. A., Jangraw, D. C., Chen, G., Hall, A., Stuber, C., Gonzalez-Castillo, J.,
789   Ivanov, D., Marrett, S., Guidi, M., Goense, J., Poser, B. A. and Bandettini, P. A. (2017) 'High-
790   Resolution CBV-fMRI Allows Mapping of Laminar Activity and Connectivity of Cortical Input

and Output in Human M1', *Neuron,* 96(6), pp. 1253-1263 e7. doi: 10.1016/j.neuron.2017.11.005

Huber, L., Tse, D. H. Y., Wiggins, C. J., Uludag, K., Kashyap, S., Jangraw, D. C., Bandettini, P. A., Poser, B. A. and Ivanov, D. (2018) 'Ultra-high resolution blood volume fMRI and BOLD fMRI in humans at 9.4T: Capabilities and challenges', *Neuroimage,* 178, pp. 769-779. doi: 10.1016/j.neuroimage.2018.06.025

Huber, L. R., Poser, B. A., Bandettini, P. A., Arora, K., Wagstyl, K., Cho, S., Goense, J., Nothnagel, N., Morgan, A. T., van den Hurk, J., Muller, A. K., Reynolds, R. C., Glen, D. R., Goebel, R. and Gulban, O. F. (2021b) 'LayNii: A software suite for layer-fMRI', *Neuroimage,* 237, pp. 118091. doi: 10.1016/j.neuroimage.2021.118091

Huotari, N., Raitamaa, L., Helakari, H., Kananen, J., Raatikainen, V., Rasila, A., Tuovinen, T., Kantola, J., Borchardt, V., Kiviniemi, V. J. and Korhonen, V. O. (2019) 'Sampling Rate Effects on Resting State fMRI Metrics', *Front Neurosci,* 13, pp. 279. doi: 10.3389/fnins.2019.00279

Jurkiewicz, M. T., Crawley, A. P. and Mikulis, D. J. (2018) 'Is Rest Really Rest? Resting-State Functional Connectivity During Rest and Motor Task Paradigms', *Brain Connect,* 8(5), pp. 268-275. doi: 10.1089/brain.2017.0495

Kashyap, S., Ivanov, D., Havlicek, M., Poser, B. A. and Uludag, K. (2018a) 'Impact of acquisition and analysis strategies on cortical depth-dependent fMRI', *Neuroimage,* 168, pp. 332-344. doi: 10.1016/j.neuroimage.2017.05.022

Kashyap, S., Ivanov, D., Havlicek, M., Sengupta, S., Poser, B. A. and Uludag, K. (2018b) 'Resolving laminar activation in human V1 using ultra-high spatial resolution fMRI at 7T', *Sci Rep,* 8(1), pp. 17063. doi: 10.1038/s41598-018-35333-3

Kay, K., Jamison, K. W., Vizioli, L., Zhang, R., Margalit, E. and Ugurbil, K. (2019) 'A critical assessment of data quality and venous effects in sub-millimeter fMRI', *Neuroimage,* 189, pp. 847-869. doi: 10.1016/j.neuroimage.2019.02.006

Kay, K., Jamison, K. W., Zhang, R. Y. and Ugurbil, K. (2020) 'A temporal decomposition method for identifying venous effects in task-based fMRI', *Nat Methods,* 17(10), pp. 1033-1039. doi: 10.1038/s41592-020-0941-6

Krupa, D. J., Wiest, M. C., Shuler, M. G., Laubach, M. and Nicolelis, M. A. (2004) 'Layer-specific somatosensory cortical activation during active tactile discrimination', *Science,* 304(5679), pp. 1989-92. doi: 10.1126/science.1093318

Larkum, M. E. (2013) 'The yin and yang of cortical layer 1', *Nat Neurosci,* 16(2), pp. 114-5. doi: 10.1038/nn.3317

Larkum, M. E., Petro, L. S., Sachdev, R. N. S. and Muckli, L. (2018) 'A Perspective on Cortical Layering and Layer-Spanning Neuronal Elements', *Front Neuroanat,* 12, pp. 56. doi: 10.3389/fnana.2018.00056

Lawrence, S. J. D., Formisano, E., Muckli, L. and de Lange, F. P. (2019) 'Laminar fMRI: Applications for cognitive neuroscience', *Neuroimage,* 197, pp. 785-791. doi: 10.1016/j.neuroimage.2017.07.004

Logothetis, N. K. (2002) 'The neural basis of the blood-oxygen-level-dependent functional magnetic resonance imaging signal', *Philos Trans R Soc Lond B Biol Sci,* 357(1424), pp. 1003-37. doi: 10.1098/rstb.2002.1114

Logothetis, N. K., Pauls, J., Augath, M., Trinath, T. and Oeltermann, A. (2001) 'Neurophysiological investigation of the basis of the fMRI signal', *Nature,* 412(6843), pp. 150-7. doi: 10.1038/35084005

Lu, H., Golay, X., Pekar, J. J. and Van Zijl, P. C. (2003) 'Functional magnetic resonance imaging based on changes in vascular space occupancy', *Magn Reson Med,* 50(2), pp. 263-74. doi: 10.1002/mrm.10519

839 Mao, T., Kusefoglu, D., Hooks, B. M., Huber, D., Petreanu, L. and Svoboda, K. (2011) 'Long-range
840   neuronal circuits underlying the interaction between sensory and motor cortex', *Neuron,* 72(1),
841   pp. 111-23. doi: 10.1016/j.neuron.2011.07.029

842 Markuerkiaga, I., Barth, M. and Norris, D. G. (2016) 'A cortical vascular model for examining the
843   specificity of the laminar BOLD signal', *Neuroimage,* 132, pp. 491-498. doi:
844   10.1016/j.neuroimage.2016.02.073

845 Marquardt, I., Schneider, M., Gulban, O. F., Ivanov, D. and Uludag, K. (2018) 'Cortical depth profiles
846   of luminance contrast responses in human V1 and V2 using 7 T fMRI', *Hum Brain Mapp,* 39(7),
847   pp. 2812-2827. doi: 10.1002/hbm.24042

848 Menon, R. S. (2002) 'Postacquisition suppression of large-vessel BOLD signals in high-resolution
849   fMRI', *Magn Reson Med,* 47(1), pp. 1-9. doi: 10.1002/mrm.10041

850 Michelson, N. J. and Kozai, T. D. Y. (2018) 'Isoflurane and ketamine differentially influence
851   spontaneous and evoked laminar electrophysiology in mouse V1', *J Neurophysiol,* 120(5), pp.
852   2232-2245. doi: 10.1152/jn.00299.2018

853 Mishra, A., Majumdar, S., Wang, F., Wilson, G. H., 3rd, Gore, J. C. and Chen, L. M. (2019) 'Functional
854   connectivity with cortical depth assessed by resting state fMRI of subregions of S1 in squirrel
855   monkeys', *Hum Brain Mapp,* 40(1), pp. 329-339. doi: 10.1002/hbm.24375

856 Moerel, M., De Martino, F., Ugurbil, K., Yacoub, E. and Formisano, E. (2019) 'Processing complexity
857   increases in superficial layers of human primary auditory cortex', *Sci Rep,* 9(1), pp. 5502. doi:
858   10.1038/s41598-019-41965-w

859 Muckli, L., De Martino, F., Vizioli, L., Petro, L. S., Smith, F. W., Ugurbil, K., Goebel, R. and Yacoub,
860   E. (2015) 'Contextual Feedback to Superficial Layers of V1', *Curr Biol,* 25(20), pp. 2690-5.
861   doi: 10.1016/j.cub.2015.08.057

862 Murphy, K., Birn, R. M. and Bandettini, P. A. (2013) 'Resting-state fMRI confounds and cleanup',
863   *Neuroimage,* 80, pp. 349-59. doi: 10.1016/j.neuroimage.2013.04.001

864 Ogawa, S., Lee, T. M., Kay, A. R. and Tank, D. W. (1990) 'Brain magnetic resonance imaging with
865   contrast dependent on blood oxygenation', *Proc Natl Acad Sci U S A,* 87(24), pp. 9868-72. doi:
866   10.1073/pnas.87.24.9868

867 Pais-Roldán, P. Y., SD and Shah, JN. (2022) 'Pre-processing of Sub-millimeter GE-BOLD fMRI Data
868   for Laminar Applications', *Front. Neuroimaging,* 1(869454). doi: doi:
869   10.3389/fnimg.2022.869454

870 Palomero-Gallagher, N. and Zilles, K. (2019) 'Cortical layers: Cyto-, myelo-, receptor- and synaptic
871   architecture in human cortical areas', *Neuroimage,* 197, pp. 716-741. doi:
872   10.1016/j.neuroimage.2017.08.035

873 Petridou, N. and Siero, J. C. W. (2019) 'Laminar fMRI: What can the time domain tell us?', *Neuroimage,*
874   197, pp. 761-771. doi: 10.1016/j.neuroimage.2017.07.040

875 Polimeni, J., Witzel,T.,and Fischl, B. (2010) 'Identifying common-source driven correlations in resting-
876   state fMRI via laminar-specific analysis in the human visual cortex', *Proc Intl Soc Mag Reson*
877   *Med,* 18, pp. 353. doi:

878 Polimeni, J. R., Fischl, B., Greve, D. N. and Wald, L. L. (2010) 'Laminar analysis of 7T BOLD using
879   an imposed spatial activation pattern in human V1', *Neuroimage,* 52(4), pp. 1334-46. doi:
880   10.1016/j.neuroimage.2010.05.005

881 Poplawsky, A. J., Fukuda, M., Murphy, M. and Kim, S. G. (2015) 'Layer-Specific fMRI Responses to
882   Excitatory and Inhibitory Neuronal Activities in the Olfactory Bulb', *J Neurosci,* 35(46), pp.
883   15263-75. doi: 10.1523/JNEUROSCI.1015-15.2015

884 Raichle, M. E., MacLeod, A. M., Snyder, A. Z., Powers, W. J., Gusnard, D. A. and Shulman, G. L.
885   (2001) 'A default mode of brain function', *Proc Natl Acad Sci U S A,* 98(2), pp. 676-82. doi:
886   10.1073/pnas.98.2.676

887 Ress, D., Glover, G. H., Liu, J. and Wandell, B. (2007) 'Laminar profiles of functional activity in the
888   human brain', *Neuroimage,* 34(1), pp. 74-84. doi: 10.1016/j.neuroimage.2006.08.020
889 Rockland, K. S. (2019) 'What do we know about laminar connectivity?', *Neuroimage,* 197, pp. 772-
890   784. doi: 10.1016/j.neuroimage.2017.07.032
891 Rolls, E. T. and Mills, W. P. C. (2017) 'Computations in the deep vs superficial layers of the cerebral
892   cortex', *Neurobiol Learn Mem,* 145, pp. 205-221. doi: 10.1016/j.nlm.2017.10.011
893 Rubio-Garrido, P., Perez-de-Manzo, F., Porrero, C., Galazo, M. J. and Clasca, F. (2009) 'Thalamic input
894   to distal apical dendrites in neocortical layer 1 is massive and highly convergent', *Cereb Cortex,*
895   19(10), pp. 2380-95. doi: 10.1093/cercor/bhn259
896 Scheeringa, R. and Fries, P. (2019) 'Cortical layers, rhythms and BOLD signals', *Neuroimage,* 197, pp.
897   689-698. doi: 10.1016/j.neuroimage.2017.11.002
898 Scheeringa, R., Koopmans, P. J., van Mourik, T., Jensen, O. and Norris, D. G. (2016) 'The relationship
899   between oscillatory EEG activity and the laminar-specific BOLD signal', *Proc Natl Acad Sci U
900   S A,* 113(24), pp. 6761-6. doi: 10.1073/pnas.1522577113
901 Schweisfurth, M. A., Frahm, J., Farina, D. and Schweizer, R. (2018) 'Comparison of fMRI Digit
902   Representations of the Dominant and Non-dominant Hand in the Human Primary
903   Somatosensory Cortex', *Front Hum Neurosci,* 12, pp. 492. doi: 10.3389/fnhum.2018.00492
904 Scott, B. B., Thiberge, S. Y., Guo, C., Tervo, D. G. R., Brody, C. D., Karpova, A. Y. and Tank, D. W.
905   (2018) 'Imaging Cortical Dynamics in GCaMP Transgenic Rats with a Head-Mounted
906   Widefield Macroscope', *Neuron,* 100(5), pp. 1045-1058 e5. doi: 10.1016/j.neuron.2018.09.050
907 Sempere-Ferrandez, A., Martinez, S. and Geijo-Barrientos, E. (2019) 'Synaptic mechanisms underlying
908   the intense firing of neocortical layer 5B pyramidal neurons in response to cortico-cortical
909   inputs', *Brain Struct Funct,* 224(4), pp. 1403-1416. doi: 10.1007/s00429-019-01842-8
910 Shah NJ, a. Z. K. (2004) *Imaging process in the spatial frequency space and useful for examining the
911   properties of object*. [Online].
912 Shah, N. J., da Silva, N. A. and Yun, S. D. (2019) 'Perfusion weighted imaging using combined
913   gradient/spin echo EPIK: Brain tumour applications in hybrid MR-PET', *Hum Brain Mapp*.
914   doi: 10.1002/hbm.24537
915 Shah, N. J., Zilles, K. (2003) *Verfahren zur Untersuchung eines Objektes mittels Erfassung des
916   Ortsfrequenzraumes*. [Online].
917 Sharoh, D., van Mourik, T., Bains, L. J., Segaert, K., Weber, K., Hagoort, P. and Norris, D. G. (2019)
918   'Laminar specific fMRI reveals directed interactions in distributed networks during language
919   processing', *Proc Natl Acad Sci U S A,* 116(42), pp. 21185-21190. doi:
920   10.1073/pnas.1907858116
921 Siero, J. C., Petridou, N., Hoogduin, H., Luijten, P. R. and Ramsey, N. F. (2011) 'Cortical depth-
922   dependent temporal dynamics of the BOLD response in the human brain', *J Cereb Blood Flow
923   Metab,* 31(10), pp. 1999-2008. doi: 10.1038/jcbfm.2011.57
924 Speck, O. and Hennig, J. (1998) 'Functional imaging by I0- and T2*-parameter mapping using multi-
925   image EPI', *Magn Reson Med,* 40(2), pp. 243-8. doi: 10.1002/mrm.1910400210
926 Stanley, O. W., Kuurstra, A. B., Klassen, L. M., Menon, R. S. and Gati, J. S. (2021) 'Effects of phase
927   regression on high-resolution functional MRI of the primary visual cortex', *Neuroimage,* 227,
928   pp. 117631. doi: 10.1016/j.neuroimage.2020.117631
929 Thomson, A. M. and Bannister, A. P. (2003) 'Interlaminar connections in the neocortex', *Cereb Cortex,*
930   13(1), pp. 5-14. doi: 10.1093/cercor/13.1.5
931 Uludag, K. and Blinder, P. (2018) 'Linking brain vascular physiology to hemodynamic response in
932   ultra-high field MRI', *Neuroimage,* 168, pp. 279-295. doi: 10.1016/j.neuroimage.2017.02.063
933 van Mourik, T., van der Eerden, J., Bazin, P. L. and Norris, D. G. (2019) 'Laminar signal extraction
934   over extended cortical areas by means of a spatial GLM', *PLoS One,* 14(3), pp. e0212493. doi:
935   10.1371/journal.pone.0212493

Viessmann, O., Scheffler, K., Bianciardi, M., Wald, L. L. and Polimeni, J. R. (2019) 'Dependence of resting-state fMRI fluctuation amplitudes on cerebral cortical orientation relative to the direction of B0 and anatomical axes', *Neuroimage,* 196, pp. 337-350. doi: 10.1016/j.neuroimage.2019.04.036

Waehnert, M. D., Dinse, J., Weiss, M., Streicher, M. N., Waehnert, P., Geyer, S., Turner, R. and Bazin, P. L. (2014) 'Anatomically motivated modeling of cortical laminae', *Neuroimage,* 93 Pt 2, pp. 210-20. doi: 10.1016/j.neuroimage.2013.03.078

Weiler, N., Wood, L., Yu, J., Solla, S. A. and Shepherd, G. M. (2008) 'Top-down laminar organization of the excitatory network in motor cortex', *Nat Neurosci,* 11(3), pp. 360-6. doi: 10.1038/nn2049

Whitesell, J. D., Liska, A., Coletta, L., Hirokawa, K. E., Bohn, P., Williford, A., Groblewski, P. A., Graddis, N., Kuan, L., Knox, J. E., Ho, A., Wakeman, W., Nicovich, P. R., Nguyen, T. N., van Velthoven, C. T. J., Garren, E., Fong, O., Naeemi, M., Henry, A. M., Dee, N., Smith, K. A., Levi, B., Feng, D., Ng, L., Tasic, B., Zeng, H., Mihalas, S., Gozzi, A. and Harris, J. A. (2021) 'Regional, Layer, and Cell-Type-Specific Connectivity of the Mouse Default Mode Network', *Neuron,* 109(3), pp. 545-559 e8. doi: 10.1016/j.neuron.2020.11.011

Wiggins, C. a. N., DG (2000) 'Investigation of inflow effects on fMR1 at 3T', *Proc. Intl. Sot. Mag. Reson. Med.,* 8, pp. 942. doi:

Xu, T., Yang, Z., Jiang, L., Xing, X., Zuo, X. (2015) 'A Connectome Computation System for discovery science of brain', *Science Bulletin,* 60(1), pp. 89-95. doi: https://doi.org/10.1007/s11434-014-0698-3

Xue, S. W., Li, D., Weng, X. C., Northoff, G. and Li, D. W. (2014) 'Different neural manifestations of two slow frequency bands in resting functional magnetic resonance imaging: a systemic survey at regional, interregional, and network levels', *Brain Connect,* 4(4), pp. 242-55. doi: 10.1089/brain.2013.0182

Yacoub, E., Harel, N. and Ugurbil, K. (2008) 'High-field fMRI unveils orientation columns in humans', *Proc Natl Acad Sci U S A,* 105(30), pp. 10607-12. doi: 10.1073/pnas.0804110105

Yu, X., Qian, C., Chen, D. Y., Dodd, S. J. and Koretsky, A. P. (2014) 'Deciphering laminar-specific neural inputs with line-scanning fMRI', *Nat Methods,* 11(1), pp. 55-8. doi: 10.1038/nmeth.2730

Yuen, N. H., Osachoff, N. and Chen, J. J. (2019) 'Intrinsic Frequencies of the Resting-State fMRI Signal: The Frequency Dependence of Functional Connectivity and the Effect of Mode Mixing', *Front Neurosci,* 13, pp. 900. doi: 10.3389/fnins.2019.00900

Yun, S., Pais-Roldán, P., Palomero-Gallagher, N., Shah, N. J. (2022) 'Mapping of Whole-Brain Resting-State Networks with HalfMillimetre Resolution', *Human Brain Mapping.* doi: 10.1002/hbm.25855

Yun, S., Pais-Roldan, P., Shah, NJ. (2020) 'Detection of Cortical Depth-dependent Functional Activation using Whole-brain, Half-millimetre Resolution EPIK at 7T', *ISMRM, Sydney, Australia.* doi:

Yun, S. and Shah, N. J. 'Full-FOV, Whole-brain, Half-millimetre Resolution fMRI at 7T using Accelerated multi-band EPIK with TR-external Phase Correction', *27th Annual Meeting of ISMRM*, Montreal, Canada.

Yun, S. D., Pais-Roldan, P., Palomero-Gallagher, N. and Shah, N. J. (2022) 'Mapping of whole-cerebrum resting-state networks using ultra-high resolution acquisition protocols', *Hum Brain Mapp.* doi: 10.1002/hbm.25855

Yun, S. D., Reske, M., Vahedipour, K., Warbrick, T. and Shah, N. J. (2013) 'Parallel imaging acceleration of EPIK for reduced image distortions in fMRI', *Neuroimage,* 73, pp. 135-43. doi: 10.1016/j.neuroimage.2013.01.070

Yun, S. D. and Shah, N. J. (2017) 'Whole-brain high in-plane resolution fMRI using accelerated EPIK for enhanced characterisation of functional areas at 3T', *PLoS One,* 12(9), pp. e0184759. doi: 10.1371/journal.pone.0184759

985 Yun, S. D. and Shah, N. J. (2020) 'Analysis of EPI phase correction with low flip-angle excitation to
986   reduce the required minimum TE: Application to whole-brain, submillimeter-resolution fMRI
987   at 3 T', *Magn Reson Med,* 84(3), pp. 1416-1429. doi: 10.1002/mrm.28218
988 Yun, S. D., Weidner, R., Weiss, P. H. and Shah, N. J. (2019) 'Evaluating the Utility of EPIK in a Finger
989   Tapping fMRI Experiment using BOLD Detection and Effective Connectivity', *Sci Rep,* 9(1),
990   pp. 10978. doi: 10.1038/s41598-019-47341-y
991 Zaitsev, M., D'Arcy, J., Collins, D. J., Leach, M. O., Zilles, K. and Shah, N. J. (2005) 'Dual-contrast
992   echo planar imaging with keyhole: application to dynamic contrast-enhanced perfusion studies',
993   *Phys Med Biol,* 50(19), pp. 4491-505. doi: 10.1088/0031-9155/50/19/005
994 Zaitsev, M., Zilles, K. and Shah, N. J. (2001) 'Shared k-space echo planar imaging with keyhole', *Magn
995   Reson Med,* 45(1), pp. 109-17. doi: 10.1002/1522-2594(200101)45:1<109::aid-
996   mrm1015>3.0.co;2-x
997 Zilles, K. and Catani, M. (2020) 'Cerebral hemispheres', *Gray's Anatomy.* 43th ed.
998 Zuo, X. N., Di Martino, A., Kelly, C., Shehzad, Z. E., Gee, D. G., Klein, D. F., Castellanos, F. X.,
999   Biswal, B. B. and Milham, M. P. (2010) 'The oscillating brain: complex and reliable',
1000   *Neuroimage,* 49(2), pp. 1432-45. doi: 10.1016/j.neuroimage.2009.09.037
1001

1002   **Tables:**

1003   **Table 1. Regions of interest.** DMN: default mode network; EXEC: executive control network; SM:
1004   sensory-motor network. ROIs extracted from the Freesurfer surface parcellation *aparc.a2009s.annot*,
1005   based on the Destrieux atlas.

Abb. ROI	Full ROI name	Related network(s)
MPCC	Posterior Midcingulate Cortex	DMN
ACC	Anterior Cingulate Cortex	DMN
PCC	Posterior Cingulate Cortex	DMN
PCUN	Precuneus	DMN & VISUAL
STS	Superior Temporal Sulcus	DMN & EXEC
PoCG	Postcentral Gyrus	EXEC & SM
ANG	Inferior Parietal - angular	EXEC
SMG	Inferior Parietal - supramarginal	EXEC
IFG	Inferior Frontal G&S	EXEC
MFG	Middle Frontal Gyrus	EXEC
SFG	Superior Frontal G&S	EXEC & SM
SOG	Superior Occipital Gyrus	VISUAL
POS	Parieto-occipital Sulcus	VISUAL
CAL	Calcarine	VISUAL
CUN	Cuneus	VISUAL
CS	Central Sulcus	SM
PreCG	Precentral Gyrus	SM
PreCS	Precentral Sulcus	SM
STG	Superior Temporal Gyrus	AUDITORY
SubCG	Subcentral G&S	AUDITORY
MACG	Anterior Midcingulate Cortex	SALIENCE

1006

1007

31

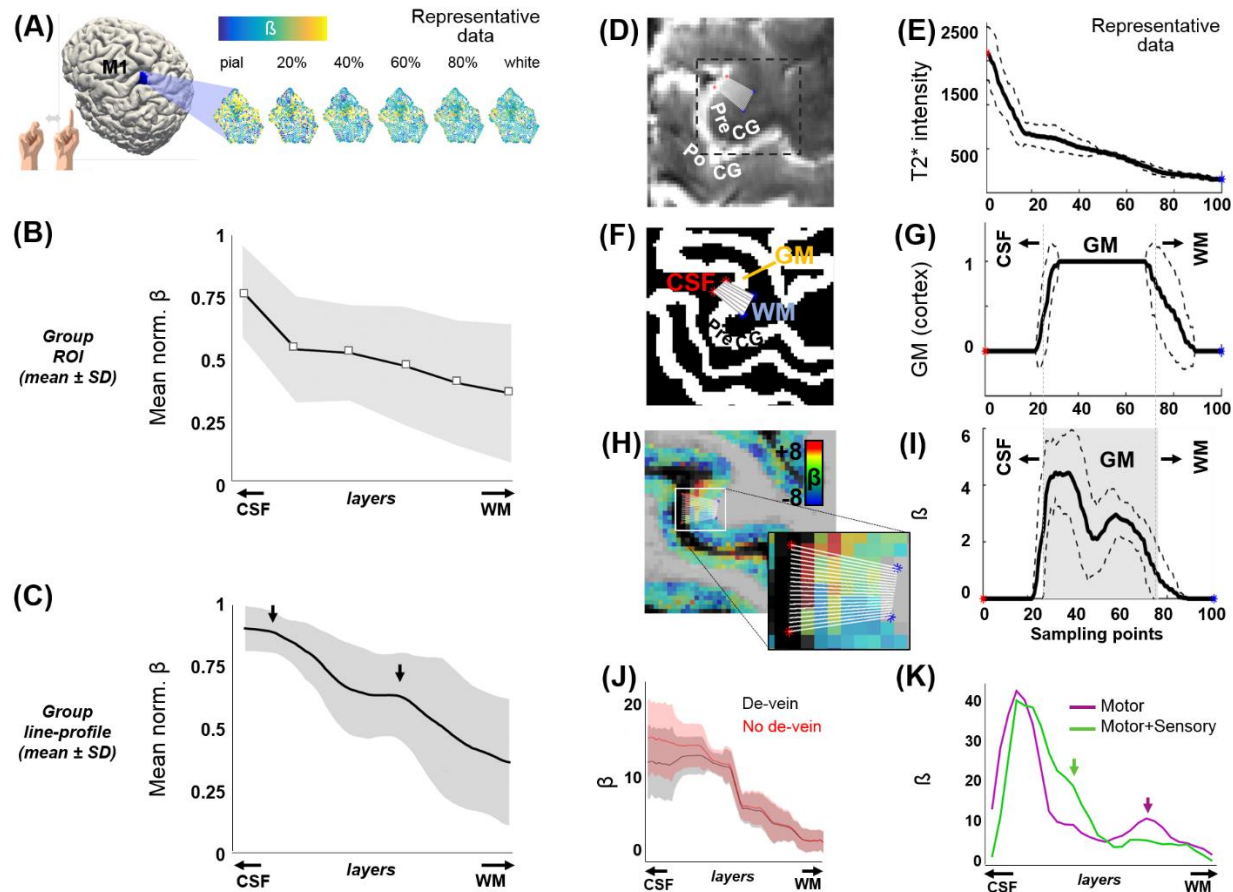1008 **Figures and figure legends:**

1009

1010 *Fig. 1. Cortical depth-dependent motor task-evoked BOLD fMRI. (**A**) Flattened patches of M1 extracted from*
1011 *six surfaces at different cortical depths in one volunteer. (**B**) The plot shows the mean ±SD of the normalized*
1012 *beta-coefficient in six cortical patches of M1 at different cortical depths (N=13). (**C**) Mean ±SD of the*
1013 *normalized activation line-profiles, computed from the beta map of 13 subjects, using a line-profile method on*
1014 *a particular segment of M1 (computation explained through panels (D)-(I)) The arrows point to the two main*
1015 *activation peaks observed along the cortical depth. (**D**) The figure shows part of a mean TR-external EPIK axial*
1016 *slice containing the precentral gyrus (PreCG). The 20 overlaid sampling lines (in white) extend from the CSF,*
1017 *covering the cortical thickness, up to the WM. (**E**) Average line profile of the mean TR-external EPIK on the*
1018 *selected sampling region. Note the high intensity at the initial points (CSF, with long T2 constant). The dashed*
1019 *lines above and below the solid line represent the mean ±SD. (**F**) Same region as in (D), cropped from the*
1020 *segmented MP2RAGE, which identifies the cortical ribbon (in white color, labeled as GM). (**G**) Line profile*
1021 *calculated from the sampling lines over the image in (F). (**H**) Beta coefficient map overlaid on the MP2RAGE*
1022 *and zoomed view of the 20 sampling lines. (**I**) Profile of the beta coefficient along the selected lines crossing the*
1023 *finger motor area in the PreCG. Note the higher signal on superficial and middle layers of the cerebral cortex*
1024 *(double peak, typical of motor tasks). The gray-shaded area in i) represents the extent of the GM, with superficial*

32

1025   *layers (near the CSF) on the left and deep layers (near the WM), on the right. (**J**) An example of an evoked line*

1026   *profile computed before (red) and after (black) the addition of the de-vein correction step. (**K**) Line profiles in*

1027   *a subject performing either finger movement only (purple trace) or finger movement involving touch (green*

1028   *trace). In panels (E), (G), (I), and (K), the x-axis refers to the distance from the CSF to the WM, equidistantly*

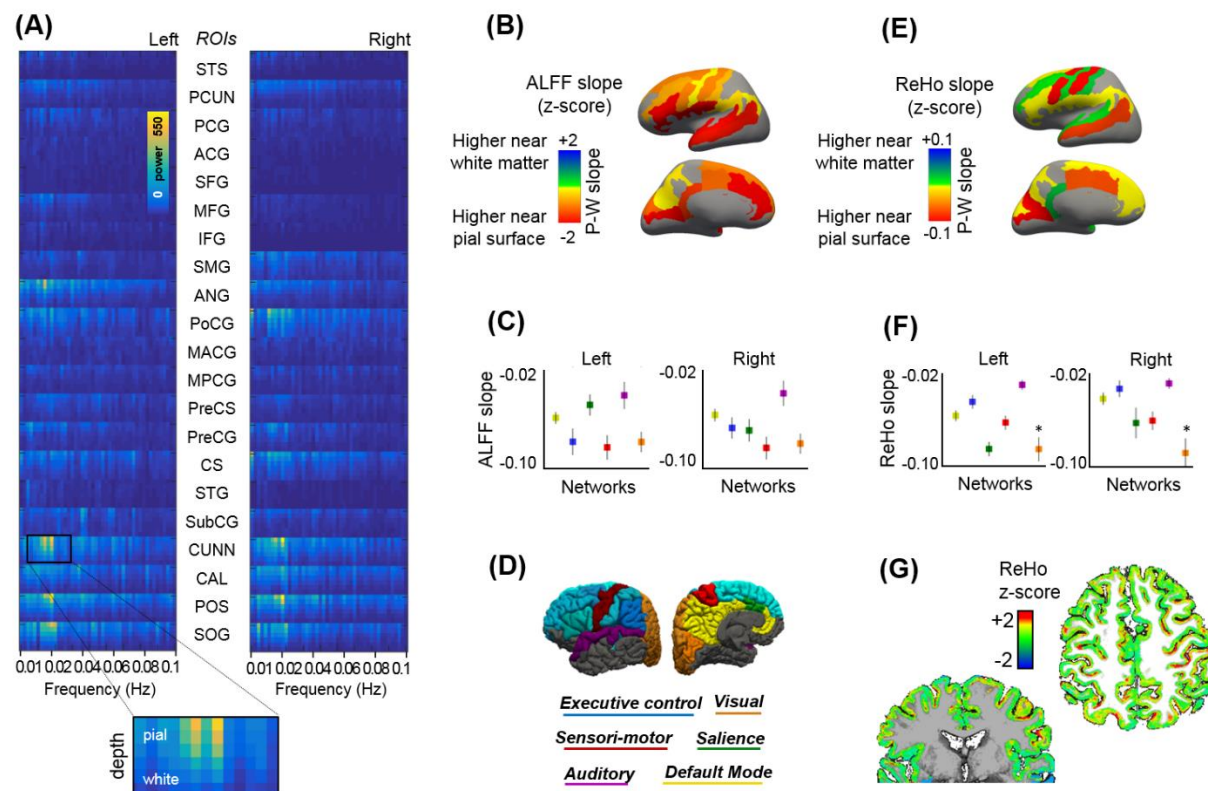1029   *sampled with 100 points.*

1030

1031

1032 ***Fig. 2. Cortical depth-dependent resting-state activity.*** *(**A**) Mean layer-specific frequency-power decomposition*
1033 *of the BOLD signal in 21 ROIs (both cerebral hemispheres), averaged across 13 subjects. (**B**) Brain surface*
1034 *maps showing the average slope of the fitting line that best approaches the depth-varying ALFF per ROI. (**C**)*
1035 *ALFF slope for each cortical network. (**D**) The figure displays the regions that were included in the functional*
1036 *analysis, organized by network, over the surface of the brain (see **Table 1** for a detailed description of the ROIs*
1037 *included). (**E**) Brain surface maps showing the average ReHo slope of the fitting line that best approaches the*
1038 *depth-varying ReHo per ROI. (**F**) ReHo slope for each cortical network. (**G**) Representative ReHo map projected*
1039 *from six cortical surfaces to volume space. Results based on equi-distant layer sampling (for a comparison of*
1040 *ALFF and ReHo results in the whole-brain, gyri, and sulci when using an equi-distance or an equi-volume*
1041 *sampling model, see **Figures S7** and **S8**).*

1042

1043
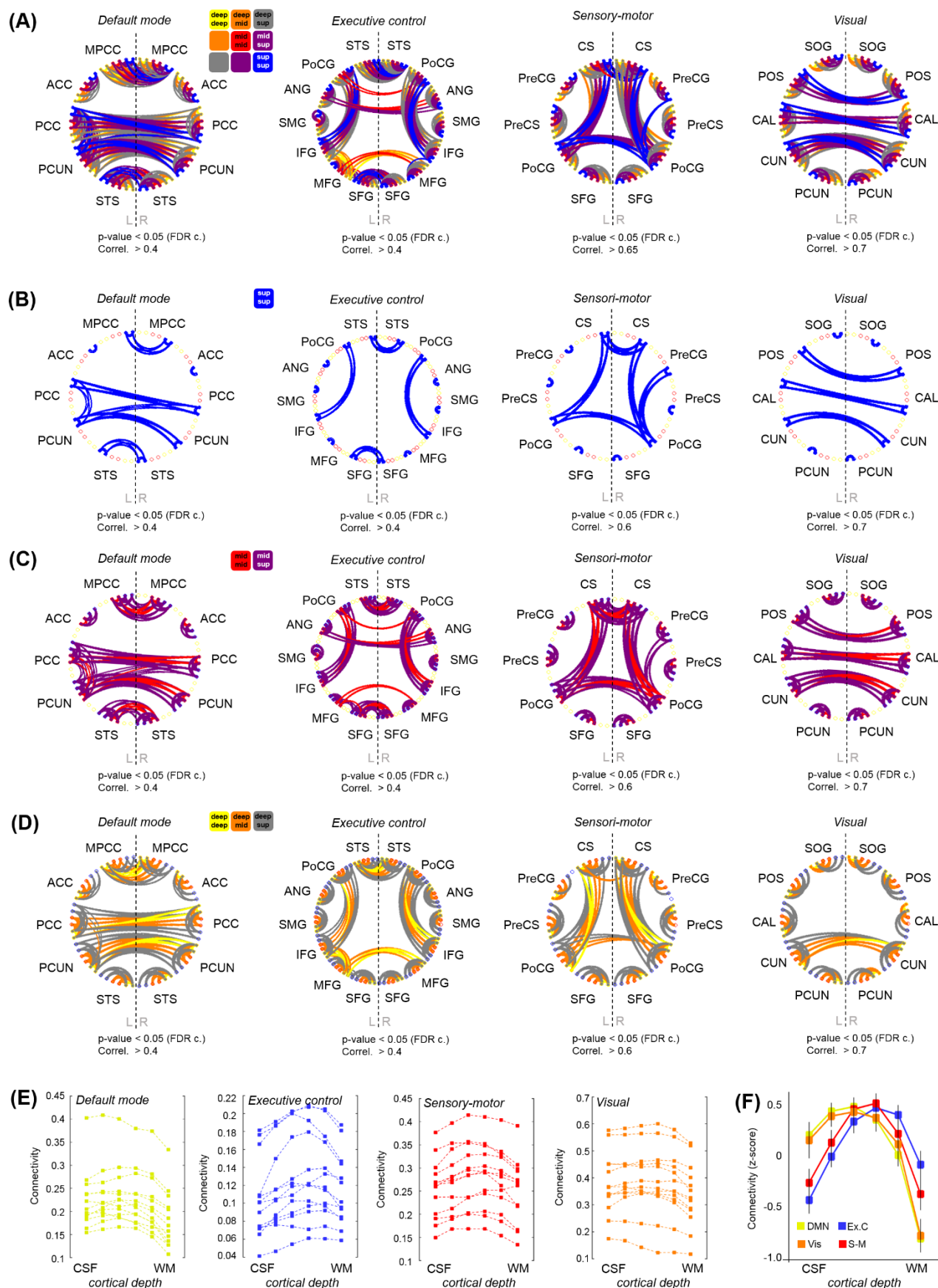
1044   ***Fig. 3. Cortical depth-dependent functional connectivity.** (**A**) Four graphs showing the layer-specific*

1045   *functional connections between ROIs engaged in four different brain networks. A legend is provided above the*

1046   *first graph. A version of these graphs hiding the different layers is provided in (**B**), (**C**), and (**D**). (**E**) Each of*

1047   *the four graphs shows the averaged connectivity (temporal correlation) within each functional network at each*

1048   *cortical depth for all subjects included in the analysis. (**F**) Cortical depth-specific global connectivity averaged*

1049   *in four resting-state networks (after transforming subject connectivity values to z-score). Error bars indicate ±*

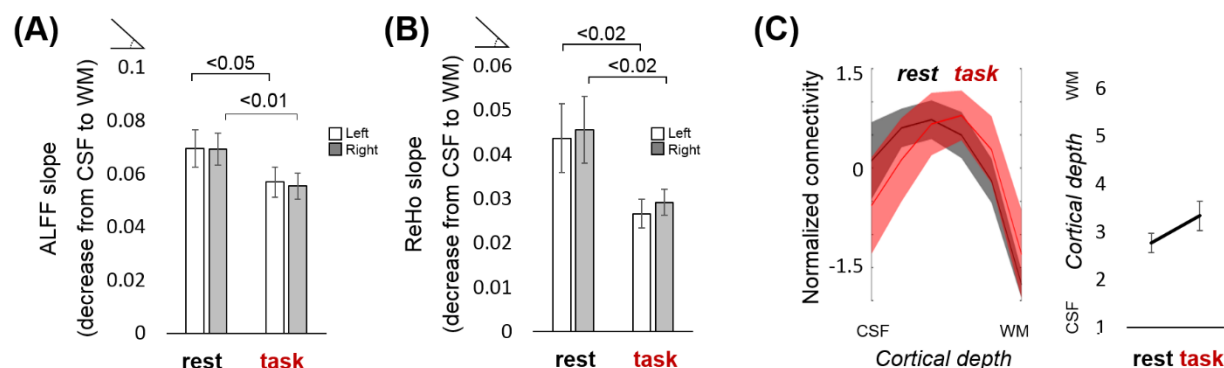1050   *standard error of the mean, N=13.*

1051

Fig. 4. Functional laminar differences between resting state and task. *(A) The bar plot represents the average ALFF slope computed for the resting-state and the task scan (after regressing out the estimated task response). (B) Average ReHo slope computed for the resting-state and the task scan (after regressing out the estimated task response). Values above the horizontal lines refer to the p-value of a t-test between conditions. (C) (left:) Normalized mean ± standard error of the laminar connectivity profile in the DMN during rest (black trace) and task (red trace), overlaid for comparison, and (right:) mean cortical depth at which the connectivity is maximum for each condition (not significantly different; the p-value of a t-test between conditions was 0.16). Error bars represent the standard error of the mean. N=13 for rs-fMRI-1 ("rest"); N=12 for task-fMRI ("task").*